



A Luminous X-Ray Transient in SDSS J143359.16+400636.0: A Likely Tidal Disruption Event

Murray Brightman¹ , Charlotte Ward², Daniel Stern³ , Kunal Mooley¹ , Kishalay De¹, Suvi Gezari^{2,4} ,

Sjoert Van Velzen^{2,5} , Igor Andreoni⁶, Matthew Graham¹ , Frank J. Masci⁷ , Reed Riddle¹ , and Jeffry Zolkower⁸

¹ Cahill Center for Astrophysics, California Institute of Technology, 1216 East California Boulevard, Pasadena, CA 91125, USA; murray@srl.caltech.edu

² Department of Astronomy, University of Maryland, College Park, MD 20742, USA

³ Jet Propulsion Laboratory, California Institute of Technology, Pasadena, CA 91109, USA

⁴ Joint Space-Science Institute, University of Maryland, College Park, MD 20742, USA

⁵ Center for Cosmology and Particle Physics, New York University, New York, NY 10003, USA

⁶ Division of Physics, Mathematics and Astronomy, California Institute of Technology, Pasadena, CA 91125, USA

⁷ IPAC, California Institute of Technology, 1200 East California Boulevard, Pasadena, CA 91125, USA

⁸ Caltech Optical Observatories, California Institute of Technology, Pasadena, CA 91125, USA

Received 2020 October 23; revised 2021 January 8; accepted 2021 January 16; published 2021 March 10

Abstract

We present the discovery of a luminous X-ray transient, serendipitously detected by Swift’s X-ray Telescope on 2020 February 5, located in the nucleus of the galaxy SDSS J143359.16+400636.0 at $z = 0.099$ (luminosity distance $D_L = 456$ Mpc). The transient was observed to reach a peak luminosity of $\sim 10^{44}$ erg s $^{-1}$ in the 0.3–10 keV X-ray band, which was ~ 20 times more than the peak optical/UV luminosity. Optical, UV, and X-ray light curves from the Zwicky Transient Facility and Swift show a decline in flux from the source consistent with $t^{-5/3}$, and observations with NuSTAR and Chandra show a soft X-ray spectrum with photon index $\Gamma = 2.9 \pm 0.1$. The X-ray/UV properties are inconsistent with well-known active galactic nucleus properties and have more in common with known X-ray tidal disruption events (TDEs), leading us to conclude that it was likely a TDE. The broadband spectral energy distribution can be described well by a disk blackbody model with an inner disk temperature of $7.3_{-0.8}^{+0.3} \times 10^5$ K, with a large fraction ($>40\%$) of the disk emission upscattered into the X-ray band. An optical spectrum taken with Keck/LRIS after the X-ray detection reveals LINER line ratios in the host galaxy, suggesting low-level accretion onto the supermassive black hole prior to the event, but no broad lines or other indications of a TDE were seen. The stellar velocity dispersion implies that the mass of the supermassive black hole powering the event is $\log(M_{\text{BH}}/M_{\odot}) = 7.41 \pm 0.41$, and we estimate that at peak the Eddington fraction of this event was $\sim 50\%$. This likely TDE was not identified by wide-field optical surveys or optical spectroscopy, indicating that more events like this would be missed without wide-field UV or X-ray surveys.

Unified Astronomy Thesaurus concepts: Tidal disruption (1696); X-ray transient sources (1852); Transient sources (1851); X-ray sources (1822); Supermassive black holes (1663)

Supporting material: data behind figure

1. Introduction

Tidal disruption events (TDEs) occur when stars in the center of a galaxy that orbit close to the supermassive black hole (SMBH) get close enough that the tidal forces acting on them exceed their own self gravity, causing the star to be disrupted. In this case a large fraction of the star’s mass can be accreted onto the black hole, producing a flare of electromagnetic radiation (e.g., Rees 1988).

TDEs provide uniquely powerful tools for determining black hole demographics and investigating super-Eddington accretion. TDE rates are generally skewed to lower-mass black holes, since the tidal disruption radius is interior of the Schwarzschild radius for $M_{\text{BH}} > 10^8 M_{\odot}$, and therefore TDEs provide a useful signpost of lower-mass SMBHs. Furthermore, for $M_{\text{BH}} < 10^7 M_{\odot}$, TDEs can emit above the Eddington luminosity (Strubbe & Quataert 2009), making them laboratories for extreme accretion.

Distinguishing TDEs from flares of more common accretion onto an SMBH can be challenging (Auchettl et al. 2018). One defining feature of TDEs is that their luminosities decline monotonically, often with a power-law profile approximately following $t^{-5/3}$, determined by the time in which the stellar debris gets accreted (Evans & Kochanek 1989).

While TDEs are regularly being discovered by wide-field optical surveys such as the Zwicky Transient Facility (ZTF; e.g., van Velzen et al. 2019) and the All-Sky Automated Survey for Supernovae (ASAS-SN; e.g., Holoiu et al. 2019), TDEs discovered in the X-rays are currently comparatively rare, although eROSITA is set to change this and has already identified a handful of candidate events (e.g., Khabibullin et al. 2020). In general, optical/UV events have cooler spectra (10^4 K) and X-ray events have hotter ones (10^5 K) (Komossa 2015).

We have recently begun a program to search through public Swift/XRT observations for transient sources. The Neil Gehrels Swift Observatory (hereafter Swift; Burrows et al. 2005) observes several tens of targets every day, many of which are monitoring observations with cadences of a few days, well suited to finding transient sources. With a field of view (FOV) of 560 arcmin 2 , Swift/XRT provides a great potential for serendipitously discovering X-ray transients in the FOVs of other targets (e.g., Soderberg et al. 2009). Furthermore, since most Swift data are downloaded from the satellite and made public within hours of the observation, this allows the opportunity to follow up promptly in real time with other observatories.

On 2020 February 5, we serendipitously detected an X-ray source in the FOV of a Swift/XRT observation of SN 2020bvc, a broad-lined Type Ic supernova in the galaxy UGC09379 (Ho et al. 2020), where no previous X-ray source had been detected. The position of the X-ray source was R.A. = $14^{\text{h}} 33^{\text{m}} 58\text{:}96$, decl. = $+40^{\circ} 06' 33\text{.}5$, with a positional uncertainty of $3\text{''}5$ (90% confidence). This is $\sim 8'$ from the supernova. The position of the X-ray source placed it in or near the galaxy SDSS J143359.16+400636.0, different from SN 2020bvc. SDSS J143359.16+400636.0 has a spectroscopic redshift of $z = 0.099$ (Section 4). Here we report on follow-up and subsequent observations of the source that lead us to conclude that it was likely an X-ray TDE.

Throughout this paper we assume the cosmological parameters $H_0 = 70 \text{ km s}^{-1} \text{ Mpc}^{-1}$, $\Omega_m = 0.27$, and $\Omega_\Lambda = 0.73$. Under this assumed cosmology, the luminosity distance to SDSS J143359.16+400636.0 at $z = 0.099$ is 456 Mpc. All uncertainties are quoted at the 90% level unless otherwise stated.

2. X-Ray Data Analysis

2.1. Swift

After the initial detection of the X-ray source, we requested follow-up observations with Swift with both the XRT and Ultraviolet/Optical Telescope (UVOT) instruments, initially with a cadence of a few days, then a few times a month. In addition to the initial detection in the first XRT observation (ObsID 00032818012), Swift has observed and detected the transient in X-rays 27 times, all in photon counting mode. Previous to this, Swift observed the position of the source 17 times, 12 times in 2013 and 5 times in 2016 where the source was not detected in X-rays. We analyze all Swift observations here.

In order to obtain an X-ray light curve of the source, we used the online tool provided by the University of Leicester⁹ (Evans et al. 2007, 2009). All products from this tool are fully calibrated and corrected for effects such as pileup and the bad columns on the CCD. The XRT light curve is shown in Figure 1. For observations where a source has zero total counts, we estimate the 90% upper limit on the count rate using a typical background count rate of $7 \times 10^{-5} \text{ counts s}^{-1}$ and Poisson statistics. At peak, the transient event was detected at a brightness two orders of magnitude greater than these upper limits.

We also used the online tool as described above to build a stacked spectrum of the source. Furthermore, for each individual observation, we extracted events of the source using the HEASOFT v6.25 tool XSELECT (Arnaud 1996). Source events were selected from a circular region with a $25''$ radius centered on the above coordinates, and a background region consisting of a larger circle external to the source region was used to extract background events. For each source spectrum, we constructed the auxiliary response file (ARF) using xrtmkarf. The relevant response matrix file (RMF) from the CALDB was used. All spectra were grouped with a minimum of 1 count per bin.

The stacked spectrum has a total exposure time of 55 ks, and the average count rate of the source is $(3.04 \pm 0.08) \times 10^{-2} \text{ counts s}^{-1}$. We initially fitted the spectrum with an absorbed power-law model, tbabs*ztbabs*powerlaw in

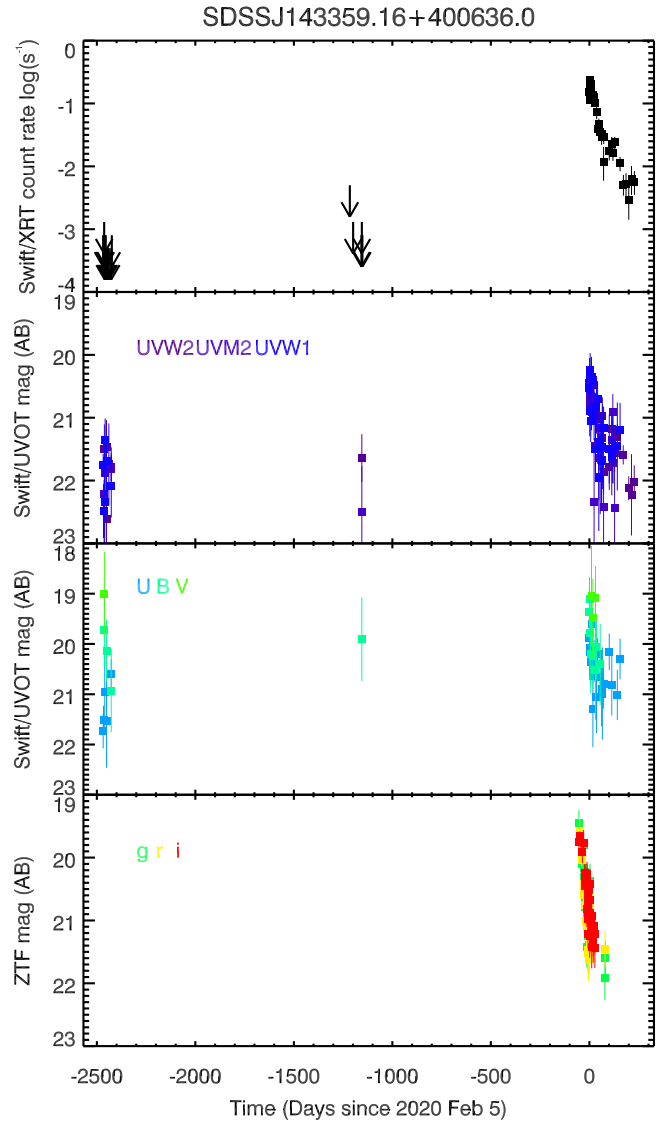


Figure 1. Long-term light curve of SDSS J143359.16+400636.0, from all Swift/XRT, Swift/UVOT, and ZTF observations. On 2020 February 5 a bright X-ray source was detected with a count rate 2 orders of magnitude greater than previous upper limits (shown by downward-pointing arrows). The host galaxy was seen in the UVOT data prior to the transient, so only a small increase in brightness was measured, and it was much less than seen in the X-rays. The ZTF data are from difference imaging (hence, the host galaxy has been subtracted) and show that the transient was detected in the optical ~ 60 days before Swift detected it in the X-rays.

XSPEC, where the tbabs model accounts for absorption in our Galaxy, fixed at $9.8 \times 10^{19} \text{ cm}^{-2}$ (HI4PI Collaboration et al. 2016), and ztbabs accounts for absorption at the redshift of the source and is left as a free parameter. We find that $N_{\text{H}} = (7 \pm 3) \times 10^{20} \text{ cm}^{-2}$ and the photon index $\Gamma = 3.0 \pm 0.2$, where $C = 252.93$ with 283 degrees of freedom (dof). We also tested a diskbb model in place of the powerlaw model, but it does not provide a good fit, where $C = 489.66$ with 283 dof. However, the addition of a diskbb component to the tbabs*ztbabs*powerlaw model does present a small improvement to the spectral fit, yielding $N_{\text{H}} = (1.1 \pm 0.1) \times 10^{21} \text{ cm}^{-2}$, the temperature of the inner disk $kT = 0.13^{+0.09}_{-0.03} \text{ keV}$, and photon index $\Gamma = 2.8 \pm 0.3$, where $C = 245.85$ with 283 dof.

⁹ https://www.swift.ac.uk/user_objects/

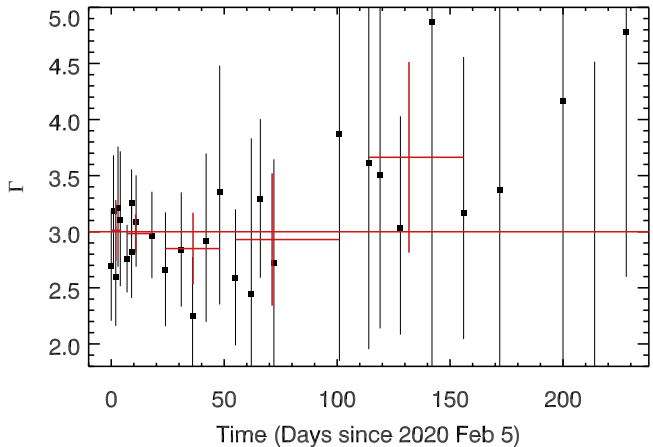


Figure 2. Power-law index, Γ , of the fit to the Swift/XRT data as a function of time (black data points). The solid red line shows the value Γ from the integrated spectrum. Also shown are binned averages where bins contain five observations each (red data points).

Subsequently, we fitted the spectra from the individual ObsIDs with the absorbed power-law model. We do not fit the more complicated model owing to the low count nature of the individual spectra. Figure 2 shows the variation in Γ over time, overplotted with binned averages (bins contain five observations each). There is no evidence of X-ray spectral evolution from the observations reported here.

The observed (absorbed) 0.3–10 keV flux as measured by XRT is 5×10^{-12} erg cm $^{-2}$ s $^{-1}$, which corresponds to a luminosity of 1×10^{34} erg s $^{-1}$ at a distance of 456 Mpc. Assuming this model, the upper limit on the X-ray luminosity prior to the transient was $\sim 10^{42}$ erg s $^{-1}$, corresponding to a >2 order-of-magnitude increase in the X-ray luminosity.

In addition to the XRT data, Swift also observed the source with its UVOT instrument, which has six filters, UVW2 (central wavelength $\lambda = 1928$ Å), UVM2 ($\lambda = 2246$ Å), UVW1 ($\lambda = 2600$ Å), U ($\lambda = 3465$ Å), B ($\lambda = 4392$ Å), and V ($\lambda = 5468$ Å). In order to extract the photometry from the UVOT data, we used the tool `uvotsource`, using circular regions with a 5" radius. Not every observation is taken with all six filters, however. We show the XRT and UVOT light curves in Figure 1. While a UVOT source was clearly seen prior to the 2020 observations, likely emission from the host galaxy, a small increase in brightness measured by UVOT can be seen in the 2020 observations, though it is much weaker than seen in the X-rays. Also shown in Figure 1 are data from ZTF, which are described in Section 3.

2.2. NuSTAR

In order to study the hard X-ray emission from the transient, we obtained Director's Discretionary Time observation on the Nuclear Spectroscopic Telescope Array (NuSTAR, ObsID 90601606002; Harrison et al. 2013), which took place on 2020 February 13, 8 days after the X-ray transient was first detected by Swift. We used the HEASOFT (v6.27) tool `nuproducts` with default parameters to extract the NuSTAR spectrum. We used a circular region with a radius of 50", centered on the peak of the emission to extract the source and a region with 100" radius to extract the background. The exposure time after filtering was 51.9 ks, from which the source was detected above background in each detector up to ~ 15 keV, with a count rate of 0.01 counts s $^{-1}$ in the 3–15 keV band.

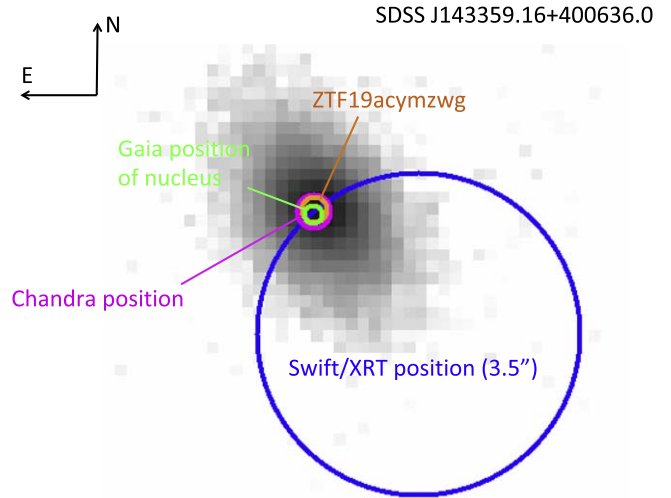


Figure 3. PanSTARRS i -band image of the galaxy SDSS J143359.16+400636.0, where the green circle shows the Gaia position of the nucleus. The position of the X-ray transient detected by Swift/XRT is shown with a blue circle, where the radius represents the 3.5" uncertainty (90% confidence), which does not clearly place the source in the galaxy. The more accurate position provided by Chandra ObsID 23172 is shown with a magenta circle (1 σ confidence) and identifies the transient with the nucleus of the galaxy. The orange circle shows the position of the related ZTF transient (1 σ confidence).

2.3. Chandra

On 2020 February 16 and 29, 11 and 24 days after the initial Swift detection, respectively, SDSS J143359.16+400636.0 was also serendipitously observed by Chandra (ObsIDs 23171 and 23172; Weisskopf 1999) for 10 ks each exposure with ACIS-S at the aim point. These observations also targeted SN 2020bvc (Ho et al. 2020). This allowed us to obtain a better position of the source than Swift/XRT provided, as well as a higher signal-to-noise ratio spectrum.

In order to determine the position of the transient, we first ran the CIAO tool `wavdetect` on the observations to obtain lists of positions for all sources in the Chandra FOV. Wavelet scales of 1, 2, 4, 8, and 16 pixels and a significance threshold of 10^{-5} were used. A total of 41 and 40 X-ray sources were detected in each observation, respectively.

We then cross-correlated the Chandra source lists with the Gaia DR2 catalog (Gaia Collaboration et al. 2018) to obtain the astrometric shifts. First, we filtered to Gaia sources within 1" of the X-ray sources, excluding the transient itself, which left five Chandra/Gaia sources from both ObsIDs. We define the astrometric shifts as the mean difference in R.A. and decl. between these matched sources. For ObsID 23171, δ R.A. = $-0.10 \pm 0.^{\circ}33$ and δ decl. = $+0.^{\circ}55 \pm 0.^{\circ}28$, and for ObsID 23172, δ R.A. = $+0.^{\circ}28 \pm 0.^{\circ}40$ and δ decl. = $+0.^{\circ}01 \pm 0.^{\circ}38$.

Having applied the astrometric shifts to the Chandra source catalog, the position of the X-ray source from ObsID 23171 is R.A. = $14^{\text{h}} 33^{\text{m}} 59^{\text{s}} 170$, decl. = $+40^{\circ} 06' 36.^{\prime\prime}18$ (J2000), with an astrometric uncertainty of 0.41" from the residual offsets with the Gaia catalog. From ObsID 23172 the position is R.A. = $14^{\text{h}} 33^{\text{m}} 59^{\text{s}} 170$, decl. = $+40^{\circ} 06' 36.^{\prime\prime}10$ (J2000), with an astrometric uncertainty of 0.37" from the residual offsets with the Gaia catalog. The Gaia position of the nucleus is R.A. = $14^{\text{h}} 33^{\text{m}} 59^{\text{s}} 170$, decl. = $+40^{\circ} 06' 36.^{\prime\prime}05$ (J2000). Figure 3 shows the PanSTARRS image of SDSS J143359.16+400636.0, with the Gaia position of the nucleus shown with

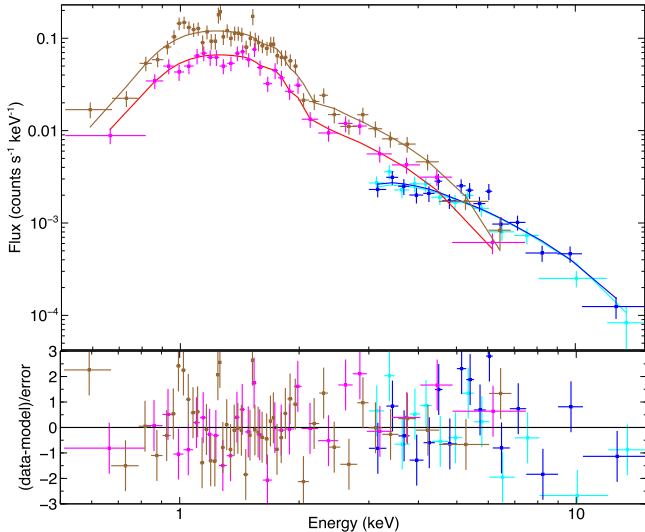


Figure 4. Chandra ObsID 23171 (brown), ObsID 23172 (magenta), NuSTAR FPMA (blue) and FPMB (cyan) spectra of the X-ray transient in SDSS J143359.16+400636.0, taken 8–24 days after the Swift/XRT detection. The data are consistent with an absorbed power law, with a constant to account for flux variability between data sets, plotted here as solid lines. The data have been binned for plotting clarity, where each bin has a minimum 5σ detection.

respect to the Chandra position of the X-ray source, which is coincident.

Also shown in Figure 3 is the position of ZTF19acymzwg, a candidate optical transient source detected in the g , r , and i bands by the ZTF on 2019 December 14, 53 days prior to the detection of the X-ray transient by Swift/XRT. We describe the analysis of the ZTF data fully in Section 3, including an updated position for the transient of R.A. = $14^{\text{h}} 33^{\text{m}} 59\rlap{.}^{\text{s}} 17$ and decl. = $+40^{\circ} 06' 36\rlap{.}^{\text{s}} 1$ with a 1σ positional uncertainty of $0\rlap{.}^{\text{s}} 29$. ZTF19acymzwg is likely related to the X-ray transient one since their positions are consistent with each other within the uncertainties.

Due to the relatively high count rate and readout time of the ACIS detectors, we check for pileup of the source using the CIAO v4.11 tool PILEUP_MAP. We find that the pileup fraction is only $\sim 2\%$ and therefore negligible. We then proceed to extract the spectrum of the source from both ObsIDs, using the CIAO tool SPECEXTRACT, and an elliptical region with a semimajor axis of $7\rlap{.}^{\text{s}} 7$ and a semiminor axis of $4\rlap{.}^{\text{s}} 4$. We used this shape and size as a result of the source being off-axis where the point-spread function is larger and elongated. Background events were extracted from a nearby region. The source was detected in the ~ 10 ks observations with a count rate of $(1.45 \pm 0.03) \times 10^{-1}$ counts s^{-1} and $(7.9 \pm 0.3) \times 10^{-2}$ counts s^{-1} , respectively, in the 0.5–8 keV band in the ACIS-S detector. There is clear evidence for a drop in flux over the 13-day period between Chandra observations. Intraobservational light curves of the Chandra observations were also extracted, binning on various timescales, though none of these showed significant count rate variability during the observations.

We jointly fitted the NuSTAR spectra with both Chandra spectra in XSPEC using the C -statistic and a cross-calibration constant included to account for cross-calibration uncertainties and flux variability. The spectra are plotted in Figure 4, which shows that they are well described by a simple absorbed power law (constant* zTbabs*powerlaw) over the 0.5–15 keV range, with $N_{\text{H}} = (9 \pm 5) \times 10^{20} \text{ cm}^{-2}$ and $\Gamma = 2.9 \pm 0.1$, where $C = 847.66$ with 883 dof, consistent with the integrated

Table 1
NuSTAR and Chandra X-Ray Spectral Fitting Results

Parameter	Result
N_{H}	$(9 \pm 5) \times 10^{20} \text{ cm}^{-2}$
Γ	2.9 ± 0.1
Normalization	$(1.2 \pm 0.2) \times 10^{-3}$
F_{X} (0.5–15 keV)	$4.0_{-0.4}^{+0.2} \times 10^{-12} \text{ erg cm}^{-2} \text{ s}^{-1}$
L_{X} (0.5–15 keV)	$9.8_{-0.4}^{+0.2} \times 10^{43} \text{ erg s}^{-1}$
C_{FPMA}	1.0 (fixed)
C_{FPMB}	1.04 (fixed)
C_{23171}	$1.36_{-0.16}^{+0.18}$
C_{23172}	0.91 ± 0.05
C -statistic	847.66
dof	883

Note. Results from the fit of an absorbed power law to the NuSTAR and Chandra spectra of the X-ray transient in SDSS J143359.16+400636.0 as measured on 2020 February 13, 8 days after the X-ray transient was first detected by Swift.

Swift spectrum. The absorption measured is in excess of the Galactic value $9.8 \times 10^{19} \text{ cm}^{-2}$ and is therefore attributable to the host.

As with the integrated Swift spectrum in Section 2.1, we fitted other spectral models to the joint Chandra and NuSTAR spectra. Again a fit with a `diskbb` model instead of a `powerlaw` model does not fit the spectrum well, with $C = 1371.92$ with 883 dof. The addition of a `diskbb` model to the `powerlaw` model does not produce an improvement to the fit, where $C = 847.12$ with 881 dof, at odds with the Swift data. Since the Swift data were integrated over all exposures, which covered a larger and later time span than the Chandra data, it is possible that this `diskbb` component emerged at later times. We checked this by creating a Swift spectrum that covered the same time period as the Chandra observations. As with the full Swift data set, the addition of the `diskbb` model to the `powerlaw` model produces an improvement to the fit, arguing against the above hypothesis and leaving the Chandra and Swift data at odds with each other. Since the Chandra data have a higher number of counts with higher signal-to-noise ratio than the Swift data, we defer to the Chandra results, concluding that there is no evidence for a `diskbb` component in addition to the power-law one.

The cross-calibration constant for NuSTAR FPMA, C_{FPMA} , is fixed to unity, while C_{FPMB} is fixed to 1.04 (Madsen et al. 2015). The constants for Chandra are $C_{23171} = 1.36_{-0.16}^{+0.18}$ and $C_{23172} = 0.91 \pm 0.05$. The 0.5–15 keV flux, as measured on 2020 February 13, 8 days after the X-ray transient was first detected by Swift, is $4.0 \times 10^{-12} \text{ erg cm}^{-2} \text{ s}^{-1}$, which corresponds to a luminosity of $9.8 \times 10^{43} \text{ erg s}^{-1}$ at a distance of 456 Mpc. These X-ray spectral fitting results are summarized in Table 1.

2.4. *e*ROSITA

Khabibullin et al. (2020) reported via The Astronomer’s Telegram (#13494) the detection by Spectrum-Roentgen-Gamma (SRG)/*e*ROSITA of a very bright X-ray source, SRGet J143359.25+400638.5, centered on SDSS J143359.16+400636.0 on 2019 December 27, 40 days prior to the detection of the transient with Swift/XRT. The reported 0.3–8 keV flux was $6.5 \times 10^{-12} \text{ erg cm}^{-2} \text{ s}^{-1}$, with no reported variability over the 11 individual scans with an interval of 4 hr.

This reported flux is almost the same flux that Swift/XRT measured, suggesting that the X-ray flux of the source remained approximately constant for at least 40 days prior to the detection by Swift/XRT, before declining, or rose and fell, or vice versa. The X-ray spectrum was reported to be soft and described by a disk blackbody spectrum with a temperature of 0.29 keV. We simulate a spectrum with these model parameters and fit with a power-law model, which yields $\Gamma = 2.9$, which is the same as measured by Swift/XRT, indicating that no spectral evolution took place between the eROSITA detection and the Swift/XRT one. The authors suggested an association with ZTF19acymzgw that we confirm here.

2.5. ROSAT

SDSS J143359.16+400636.0 was not detected by ROSAT in its all-sky survey performed in 1990 (RASS; Voges et al. 1999; Boller et al. 2016). We calculate an X-ray flux upper limit for SDSS J143359.16+400636.0 from the ROSAT data using the SOSTA (source statistics) tool available in the HEASOFT XIMAGE image processing package. The 3σ upper limit on the 0.1–2.4 keV count rate calculated using this method is 0.07 counts s^{-1} . Assuming the spectral shape measured by NuSTAR and Chandra above, this corresponds to a 0.3–10 keV flux of $1.1 \times 10^{-12} \text{ erg cm}^{-2} \text{ s}^{-1}$, which is slightly less than the peak flux of the event. This limit is also similar to that of the XMM Slew Survey (Saxton et al. 2008).

3. Zwicky Transient Facility

ZTF is an optical time-domain survey that uses the Palomar 48-inch Schmidt telescope with a 48 deg^2 FOV and scans more than 3750 deg^2 per hour to a depth of 20.5 mag (Bellm et al. 2019; Graham et al. 2019; Masci et al. 2019). As described in Section 2.3, the candidate optical transient ZTF19acymzgw was detected in the g , r , and i bands by ZTF on 2019 December 14, 53 days before the detection with Swift/XRT. Previous to this date, the field was observed on 2019 October 5 and the transient was not detected in any filter.

First, in order to determine the position of the transient, we use The Tractor (Lang et al. 2016) to forward-model the host galaxy profile and the transient point-source position. The Tractor forward-models in pixel space by parameterizing a sky noise and point-spread function model for each image and modeling this simultaneously with each source's shape, flux, and position. We apply the modeling to 49 g -, r -, and i -band ZTF images with limiting magnitude >21.5 taken from 2019 December 29 to 2020 March 28 when the transient is bright in these bands. We find that the galaxy is better modeled by a de Vaucouleurs profile than an exponential profile and that the transient point-source position is given by R.A. = $14^{\text{h}} 33^{\text{m}} 59.17^{\text{s}}$ and decl. = $+40^{\circ} 06' 36.1''$ with a 3σ positional uncertainty of $0''.61$.

Once we obtained the position of the transient, we produced ZTF light curves using the ZTF forced-photometry service (Masci et al. 2019) to produce difference-imaging photometry at the best-fit transient position across all ZTF images of the field taken between 2018 March 21 and 2020 May 11. We found no evidence for nuclear activity before the flare. The ZTF difference magnitudes are plotted in Figure 1, along with the Swift light curve.

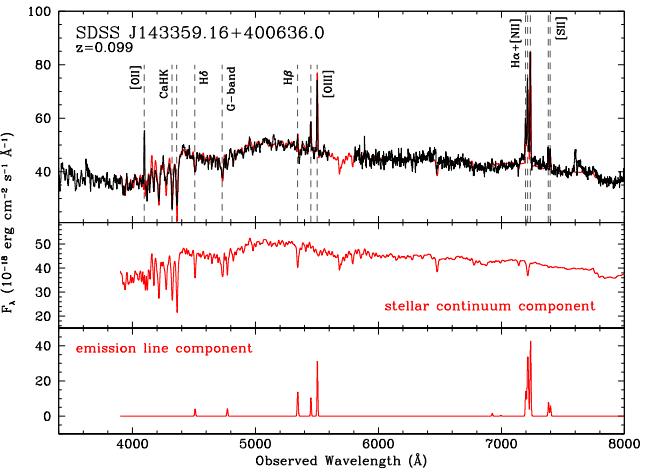


Figure 5. Keck/LRIS spectrum of the nucleus of SDSS J143359.16+400636.0 (top) taken on 2020 February 18 (black), 13 days after the X-ray transient was detected by Swift. Key emission lines are labeled. The observed spectrum is available as the data behind the figure. The model fit to the spectrum is underplotted (red), consisting of a stellar continuum component (middle) and an emission-line component (bottom).

(The data used to create this figure are available.)

4. Keck/LRIS Optical Spectroscopy

We obtained an optical spectrum of the host galaxy nucleus with Keck/LRIS (Oke et al. 1995) on 2020 February 18, 13 days after the initial Swift detection. The data were acquired using a standard long-slit mode using a $1''$ slit on both the red and blue sides when the seeing was $1''.01$ in i band. The spectra were reduced using standard long-slit reduction procedures, including flat-fielding, wavelength calibration using arcs, and flux calibration using a standard star as implemented in the `lpipe` package (Perley 2019). The spectrum is shown in Figure 5.

We proceeded to fit the Keck/LRIS spectrum in order to determine the velocity dispersion from the stellar absorption lines and the fluxes of the emission lines. We applied Penalized Pixel-Fitting (Cappellari & Emsellem 2004; Cappellari 2017) to the spectrum, which finds the velocity dispersion of stellar absorption lines using a large sample of high spectral resolution templates of single stellar populations adjusted to match the resolution of the input spectrum. We simultaneously fitted the narrow $\text{H}\alpha$, $\text{H}\beta$, $\text{H}\gamma$, $\text{H}\delta$, $[\text{S II}] \lambda\lambda 6717, 6731$, $[\text{N II}] \lambda\lambda 6550, 6585$, $[\text{O I}] \lambda\lambda 6302, 6366$, and $[\text{O III}] \lambda\lambda 5007, 4959$ emission lines during template fitting. The emission-line fluxes were each fit as free parameters, but the line widths of the Balmer series were tied to each other, as were the line widths of the forbidden lines. We show the best-fit model to the Keck/LRIS spectrum, including both the emission-line component and the stellar continuum component, in Figure 5. Equivalent widths of the lines are presented in Table 2. The redshift of the galaxy was also determined to be 0.099.

The velocity dispersion of the stellar absorption lines was determined to be $213 \pm 12 \text{ km s}^{-1}$. We used this to calculate the black hole mass from the $M_{\text{BH}}-\sigma_*$ relation, using the fit to the reverberation-mapped active galactic nucleus (AGN) sample from Woo et al. (2013), and the formula $\log(M_{\text{BH}}/M_{\odot}) = \alpha + \beta \log(\sigma_*/200 \text{ km s}^{-1})$, where $\alpha = 7.31 \pm 0.15$ and $\beta = 3.46 \pm 0.61$. The intrinsic scatter of this relation is $\epsilon = 0.41 \pm 0.05$. This yielded $\log(M_{\text{BH}}/M_{\odot}) = 7.41 \pm 0.41$. Alternatively, if we use the

Line	EW (Å)	EW Error (Å)
H δ	0.832	0.257
H γ	0.793	0.209
H β	2.575	0.429
H α	8.627	0.365
[S II] $\lambda 6716$	1.523	0.208
[S II] $\lambda 6731$	1.125	0.213
[O III] $\lambda 5007$	6.009	0.408
[O I] $\lambda 6300$	0.363	0.230
[N II] $\lambda 6583$	10.286	0.409

quiescent galaxy + AGN sample from Woo et al. (2013), where $\alpha = 8.36 \pm 0.05$ and $\beta = 4.93 \pm 0.28$ with intrinsic scatter $\epsilon = 0.43 \pm 0.04$, the black hole mass estimate is $\log(M_{\text{BH}}/M_{\odot}) = 8.49 \pm 0.43$, an order of magnitude more massive.

We then plotted the emission-line ratios [O III]/H β and [N II]/H α in Figure 6, along with the diagnostic lines from Kewley et al. (2001) and Kauffmann et al. (2003), to determine the excitation mechanism of the narrow lines. The line ratios place the nucleus of SDSS J143359.16+400636.0 in the LINER region of this diagnostic diagram, almost at the border of the Seyfert region. The stellar absorption template fitting predicted strong H β absorption, which is why we see a high [O III]/H β ratio in the initial spectrum. The lack of broad lines classifies the nucleus as a type 2 LINER. Also plotted in Figure 6 are the line ratios of nine optically and radio-selected TDE hosts (French et al. 2016, 2017; Law-Smith et al. 2017; Mattila et al. 2018; Anderson et al. 2020), along with Sloan Digital Sky Survey (SDSS) galaxies for comparison. The TDE-host and galaxy emission line flux data have been taken from the SDSS DR7 MPI-JHU catalog,¹⁰ where the stellar absorption-line spectra have also been subtracted before measurement (Kauffmann et al. 2003; Tremonti et al. 2004).

Since the narrow lines are produced in the narrow-line region, which can be kiloparsecs from the SMBH (e.g., Chen et al. 2019), this tells us that SDSS J143359.16+400636.0 had low-level AGN activity some time before the onset of the X-ray transient. To determine the spatial extent of the narrow-line region in SDSS J143359.16+400636.0, we analyzed the two-dimensional Keck/LRIS spectrum. This shows that the galaxy emission had a spatial extent of $\sim 5.2''$. We extracted a spectrum from each edge of the galaxy that was separated by a $2.4''$ gap, and each extraction region had a width of $1.4''$. In both edge spectra, we located narrow-line emission from the [O III] $\lambda\lambda 5007, 4959$ doublet. This suggests that the narrow-line emission has a spatial extent of $\sim 2.4''$. Given the scale of $1.831 \text{ kpc arcsec}^{-1}$ at this redshift under our assumed cosmology, this implies that the narrow lines were produced at a projected distance of 4.4 kpc and that they were illuminated at least 10,000 yr prior to the transient.

The flux of the [O III] line is $(3.78 \pm 0.15) \times 10^{-16} \text{ erg cm}^{-2} \text{ s}^{-1}$. From an investigation of the relationship between X-ray and optical line emission in 340 Swift/BAT-selected AGNs (Berney et al. 2015), the [O III] flux expected from the 2–10 keV flux of $10^{-12} \text{ erg cm}^{-2} \text{ s}^{-1}$, the peak X-ray flux measured by Swift/XRT, is in the range of 10^{-15} – $10^{-13} \text{ erg cm}^{-2} \text{ s}^{-1}$, higher than what we measure. The

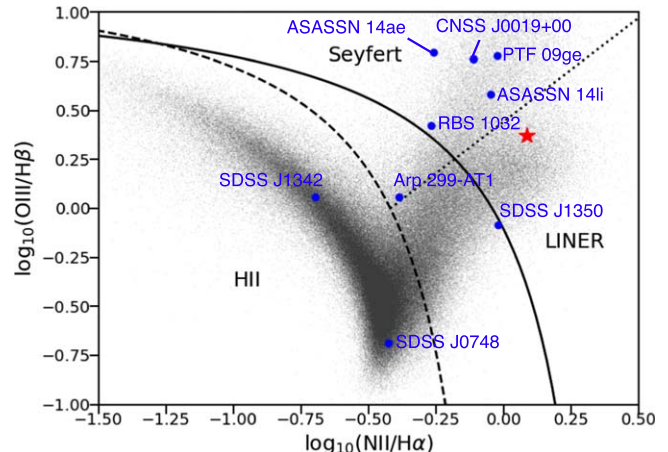


Figure 6. Emission-line ratio diagnostic diagram showing where SDSS J143359.16+400636.0 (red star) lies with respect to the Seyfert, LINER, and star-forming (HII) regions. The nucleus lies in the LINER region, indicating that AGN activity was present, at least at a low level, before the onset of the transient. For comparison, data from SDSS on optically and radio-selected TDE hosts are shown as blue circles and labeled, and other galaxies are shown in gray, where the stellar absorption-line spectrum has been subtracted.

lower-than-expected [O III] flux we measure indicates that the AGN was at a low luminosity prior to the transient. This is also consistent with the upper limits on the X-ray luminosity of the nucleus prior to the transient, which, at $\sim 10^{42} \text{ erg s}^{-1}$, is relatively low for an AGN.

5. Karl G. Jansky Very Large Array

We carried out radio observations with the Karl G. Jansky Very Large Array (VLA) through Director's Discretionary Time (project code VLA/20A-579, PI: Mooley) on 2020 August 2, 180 days after the detection by Swift. Data were obtained at C band in the 3-bit mode of the WIDAR correlator to get a contiguous frequency coverage between 4 and 8 GHz. Standard VLA calibrator sources 3C 286 and J1416+3444 were used to calibrate the flux/bandpass and phases, respectively. The data were processed using the NRAO CASA pipeline and imaged using the `clean` task in CASA.

We did not detect any radio source at the location of the transient, and we place a 3σ upper limit of $28 \mu\text{Jy}$ on the 6 GHz flux density. We can therefore place an upper limit of $4 \times 10^{37} \text{ erg s}^{-1}$ on the radio luminosity at a distance of 456 Mpc. The closest X-ray observation in time to the VLA one was by Swift/XRT on 2020 July 27 (ObsID 00013265017), where we measured a 0.3–10 keV luminosity of $3.8 \times 10^{42} \text{ erg s}^{-1}$. The X-ray-to-radio luminosity ratio is therefore $> 10^5$. Comparing our radio upper limit with the radio emission seen in jetted TDEs (e.g., Alexander et al. 2020), we can rule out the presence of a relativistic jet.

6. Light-curve Fitting

After the initial detection by Swift, the light curve of the transient appeared to monotonically decline in flux, shown by Swift, NuSTAR, Chandra, and ZTF. In order to infer more details regarding the nature of the source, we fitted the light curve of the source in each band with a power-law model, $F = A(t - t_0)^n + C$, where F is the observed flux density of the source, A is a normalization constant, t is the time in days since the transient was first detected by Swift (2020 February 5), t_0 is the inferred start time of the event in days, and n is the

¹⁰ <https://wwwmpa.mpa-garching.mpg.de/SDSS/DR7/>

Table 3
Swift/XRT and UVOT Fluxes

Time (days)	ObsID	2 keV (μ Jy)	UVW2 (mJy)	UVM2 (mJy)	UVW1 (mJy)	<i>U</i> (mJy)	<i>B</i> (mJy)	<i>V</i> (mJy)
0	00032818012	0.260 \pm 0.084	0.023 \pm 0.004	0.024 \pm 0.004	0.023 \pm 0.006	0.040 \pm 0.016	0.065 \pm 0.031	0.004 \pm 0.063
1	00032818014	0.261 \pm 0.098	0.021 \pm 0.004	0.017 \pm 0.004	0.026 \pm 0.008	0.012 \pm 0.014	0.082 \pm 0.033	...
2	00032818015	0.340 \pm 0.098	0.022 \pm 0.004	0.026 \pm 0.005	0.016 \pm 0.006	0.031 \pm 0.016	0.015 \pm 0.030	0.029 \pm 0.068
3	00032818016	0.208 \pm 0.084	0.020 \pm 0.005	0.020 \pm 0.005	0.022 \pm 0.007	0.034 \pm 0.017
4	00032818017	0.145 \pm 0.064	0.021 \pm 0.004	0.019 \pm 0.004	0.030 \pm 0.007	0.045 \pm 0.017	0.045 \pm 0.031	0.070 \pm 0.071
7	00032818018	0.333 \pm 0.068	0.017 \pm 0.003	0.024 \pm 0.004	0.014 \pm 0.004	0.026 \pm 0.011	0.030 \pm 0.022	0.034 \pm 0.060
9	00089025001	0.182 \pm 0.042	0.017 \pm 0.001
9	00032818019	0.233 \pm 0.066
11	00032818020	0.187 \pm 0.055	0.015 \pm 0.004	0.017 \pm 0.005	0.027 \pm 0.008	0.052 \pm 0.019	0.027 \pm 0.032	0.087 \pm 0.080
18	00013265001	0.208 \pm 0.057	0.019 \pm 0.003	0.025 \pm 0.005	0.025 \pm 0.005	0.011 \pm 0.008	0.029 \pm 0.017	0.058 \pm 0.042
24	00013265002	0.215 \pm 0.072	0.022 \pm 0.004	0.004 \pm 0.003	0.015 \pm 0.005	0.027 \pm 0.010	0.011 \pm 0.021	...
31	00013265003	0.159 \pm 0.056	0.009 \pm 0.002	0.002 \pm 0.003	0.009 \pm 0.005	0.020 \pm 0.009	0.022 \pm 0.020	0.084 \pm 0.049
36	00013265004	0.163 \pm 0.077	0.015 \pm 0.004	...	0.017 \pm 0.005	0.014 \pm 0.009	0.034 \pm 0.020	...
42	00013265005	0.055 \pm 0.028	0.014 \pm 0.002	0.010 \pm 0.003	0.019 \pm 0.005	0.030 \pm 0.009	0.009 \pm 0.016	...
48	00013265006	0.049 \pm 0.037	0.009 \pm 0.003	0.008 \pm 0.005	0.006 \pm 0.005	0.003 \pm 0.010	...	0.022 \pm 0.053
55	00013265007	0.067 \pm 0.027	0.012 \pm 0.003	0.006 \pm 0.003	0.010 \pm 0.004	0.020 \pm 0.009	0.025 \pm 0.019	...
62	00013265008	0.061 \pm 0.048	0.010 \pm 0.003	0.008 \pm 0.005	0.008 \pm 0.005	0.016 \pm 0.011	0.009 \pm 0.022	0.026 \pm 0.058
66	00013265009	0.038 \pm 0.021	0.014 \pm 0.004	0.009 \pm 0.004	0.010 \pm 0.006	0.015 \pm 0.012
72	00013265010	0.045 \pm 0.028	0.006 \pm 0.002	0.004 \pm 0.003	0.013 \pm 0.004	0.017 \pm 0.008	0.010 \pm 0.021	0.002 \pm 0.039
101	00013265011	0.011 \pm 0.026	0.007 \pm 0.002	...	0.009 \pm 0.005	0.032 \pm 0.011	...	0.009 \pm 0.045
114	00013265012	0.024 \pm 0.038	0.012 \pm 0.003	0.010 \pm 0.004	0.008 \pm 0.005	0.017 \pm 0.010	0.002 \pm 0.018	0.001 \pm 0.044
119	00013265013	0.018 \pm 0.018	0.007 \pm 0.002	0.016 \pm 0.004	0.009 \pm 0.005	0.007 \pm 0.009
128	00013265014	0.029 \pm 0.020	0.008 \pm 0.002	0.004 \pm 0.003	0.005 \pm 0.007	...	0.023 \pm 0.023	...
142	00013265015	0.001 \pm 0.000	0.011 \pm 0.002	...	0.010 \pm 0.006	0.014 \pm 0.007	...	0.025 \pm 0.033
156	00013265016	0.016 \pm 0.013	...	0.003 \pm 0.003	0.012 \pm 0.005	0.028 \pm 0.010	0.019 \pm 0.019	...
172	00013265017	0.007 \pm 0.012	0.008 \pm 0.001
200	00013265019	0.002 \pm 0.009	0.005 \pm 0.001
214	00013265020	0.022 \pm 0.022	0.004 \pm 0.003
228	00013265021	0.001 \pm 0.004	0.005 \pm 0.001

Note. Time is in days since 2020 February 5, the date on which the transient was first detected by Swift/XRT.

power-law index. C is a constant that represents the underlying emission from the galaxy in UVOT data only, and set to zero for the XRT data since no X-ray emission is seen from the galaxy, and set to zero for the ZTF data since the galaxy has already been subtracted in these data. We determine the underlying emission from the galaxy in the UVOT data by averaging over the photometry measured previous to the detection of the transient.

We calculate the 2 keV monochromatic flux density as measured from the power-law model fit to the NuSTAR and Chandra data with the N_{H} and Γ parameters fixed to their best-fit values. We use the UVOT flux densities as produced by `uvotsource` and the ZTF difference-imaging fluxes. We present these measurements in Tables 3 and 4.

We show a fit to the Swift/XRT, Swift/UVOT, and ZTF light curves in Figure 7, and Figure 8 shows the χ^2 contours of t_0 versus n . We find that in X-rays, to 1σ , the power-law index is consistent with $-1.1 > n > -1.9$, with a best fit of $n = -1.7$. In the UV and optical bands, the data are not as constraining and are consistent with the X-ray with, e.g., $-1.1 > n > -2.2$ for UVW2. There are indications that the transient in the UVW2 band started prior to the X-rays, where $-45 < t_0 < -5$ for X-rays and $-100 < t_0 < -20$ for UVW2, although their 1σ confidence intervals are overlapping. While the t_0 constraints from the X-rays are consistent with the eROSITA detection at $t = -40$ days, the eROSITA flux measurement is clearly not consistent with the fit to the Swift light curve, as seen in Figure 7.

For the ZTF data, we find that the power-law index is consistent with $-2.0 < n < -1.2$, and therefore with the X-ray and UV constraints, but $-100 < t_0 < -70$, which is consistent with the UV constraints but not the X-ray ones. The transient was first detected by ZTF at $t = -53$ but could have started as early as $t = -123$ owing to an observing gap. The average best fit of t_0 in the g and r bands is -70 days. If the start time of the optical transient was $t = -53$, then it would be marginally consistent with the X-ray constraints for t_0 , but in conclusion, we do not have good constraints on when the transient started, neither in X-ray nor in the optical/UV. We summarize the light-curve fitting results in Table 5.

We then assume that the optical, UV, and X-ray transients had the same start time. We do this by fixing t_0 to -70 days in all our light-curve fits, which is the best constraint from ZTF. This best fit is shown as a dashed line in Figure 7, which shows it as fitting the UVOT data well. In the X-rays, it underpredicts the XRT data between 0 and 50 days, with a flatter power-law index, $n = -1.5$. Interestingly, this model matches the eROSITA flux better.

7. SED Fitting

The Swift/UVOT and ZTF data, in combination with the Chandra and NuSTAR spectra, allow us to construct a broadband SED of the source. Since the Swift/UVOT data include emission from the host galaxy, we used the photometry inferred by the model fitting described above in Section 6. This naturally accounts for the host galaxy emission underlying the

Table 4
ZTF Fluxes

Time (Days)	<i>g</i> (mJy)	<i>r</i> (mJy)	<i>i</i> (mJy)
-53	0.060 ± 0.012	...	0.046 ± 0.006
-50	...	0.053 ± 0.010	...
-48	0.050 ± 0.004
-38	0.033 ± 0.002	0.035 ± 0.004	...
-35	0.039 ± 0.006
-30	0.036 ± 0.007	...	0.045 ± 0.008
-29	0.031 ± 0.007	0.023 ± 0.004	...
-28	...	0.022 ± 0.003	...
-24	0.024 ± 0.008
-23	0.024 ± 0.007
-22	0.023 ± 0.007	...	0.027 ± 0.004
-21	0.023 ± 0.005	0.018 ± 0.004	0.025 ± 0.003
-20	0.026 ± 0.003
-18	0.019 ± 0.003	0.014 ± 0.004	...
-14	0.013 ± 0.003
-13	0.014 ± 0.003	0.014 ± 0.004	0.017 ± 0.005
-12	...	0.018 ± 0.003	0.028 ± 0.004
-9	0.020 ± 0.003
-8	0.012 ± 0.002	0.009 ± 0.002	0.018 ± 0.003
-7	0.010 ± 0.003	0.009 ± 0.003	0.017 ± 0.004
-6	0.015 ± 0.003	0.015 ± 0.004	0.017 ± 0.005
-5	0.010 ± 0.002
-4	...	0.008 ± 0.003	0.016 ± 0.003
-2	0.023 ± 0.005
-1	0.021 ± 0.005	0.022 ± 0.004	0.016 ± 0.005
0	0.016 ± 0.005
1	0.016 ± 0.005	0.010 ± 0.003	0.014 ± 0.004
2	0.026 ± 0.006	0.012 ± 0.004	...
3	...	0.015 ± 0.005	0.022 ± 0.006
7	0.014 ± 0.003
8	...	0.012 ± 0.004	...
9	0.012 ± 0.003
10	...	0.012 ± 0.004	...
11	0.013 ± 0.003
19	0.011 ± 0.003
23	0.013 ± 0.003
27	0.011 ± 0.003
78	0.006 ± 0.002
79	...	0.010 ± 0.003	...
80	0.008 ± 0.002

Note. Time is in days since 2020 February 5, the date on which the transient was first detected by Swift/XRT.

source, which is assumed to be constant. The photometric errors were calculated by fixing all model parameters with the exception of the normalization. The SED is shown in Figure 9.

In order to fit the broadband SED, we converted the UVOT and ZTF fluxes into a PHA (pulse height amplitude) file using the tool FTFLX2XSP so that it can be loaded into XSPEC. We used the time of the NuSTAR observation to calculate the UVOT photometry and take the closest ZTF data. Using XSPEC and the χ^2 statistic for spectral fitting, we find that the ZTF and Swift/UVOT data alone can be well described by a power-law model, $F_\gamma = AE^{-\Gamma}$, where F_γ is the photon flux in units of photons $\text{cm}^{-2} \text{s}^{-1} \text{keV}^{-1}$, A is a normalization constant, E is the photon energy in keV, and Γ is the power-law index. For this model, we find $\Gamma = 1.01^{+0.41}_{-0.56}$, where $\chi^2 = 2.42$ with 6 dof. The $0.002\text{--}0.01$ keV flux is $2.2 \times 10^{-13} \text{ erg cm}^{-2} \text{s}^{-1}$, which corresponds to a luminosity of $5.1 \times 10^{42} \text{ erg s}^{-1}$ at a distance

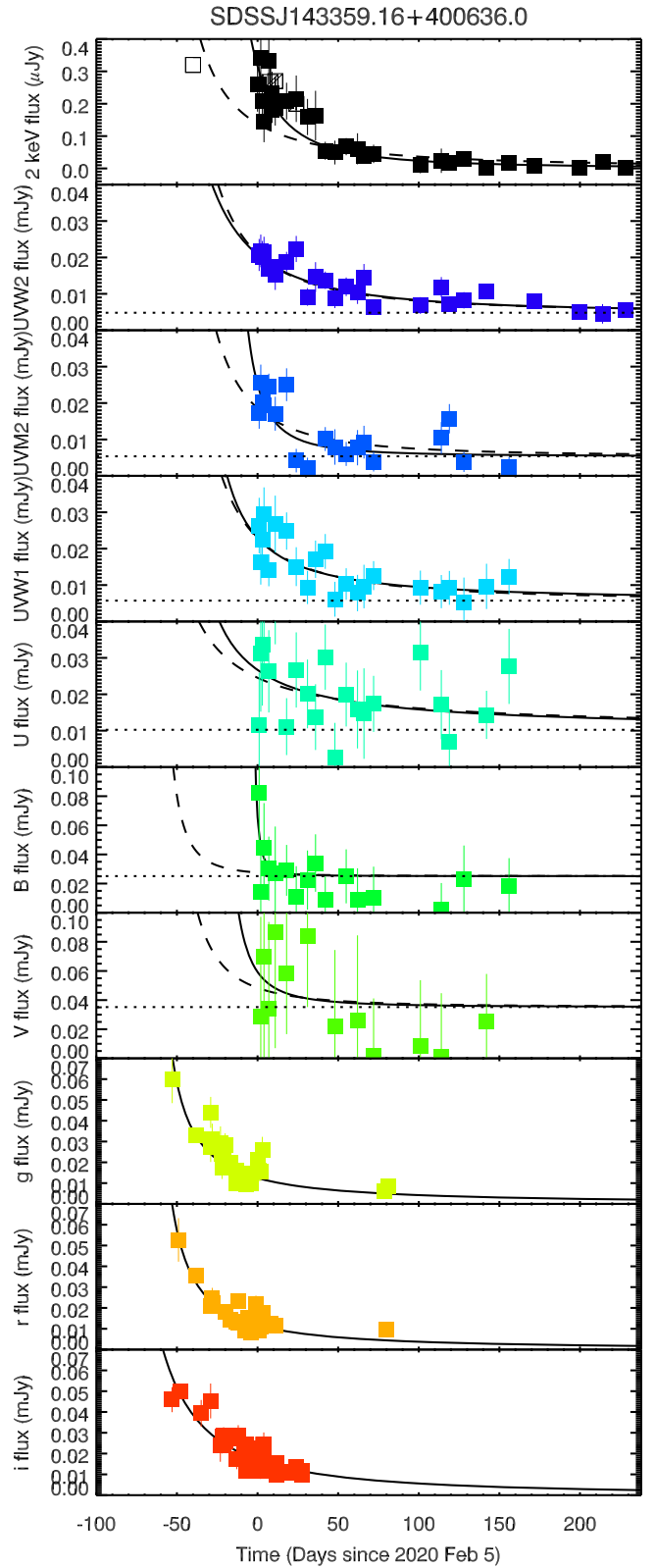


Figure 7. Swift/XRT (2 keV), Swift/UVOT (UVW2, UVM2, UVW1, *U*, *B*, and *V*), and ZTF (*g*, *r*, and *i*) light curves of the X-ray transient in SDSS J143359.16+400636.0. Solid black lines represent fits to the data with a power-law model where all fit parameters are free to vary. Dashed black lines represent fits where the start time of the transient has been fixed to -70 days. Open squares in the X-ray light curves are the data points from eROSITA, NuSTAR, and Chandra that were not used to fit the light curve. Black dotted lines show the quiescent flux from the galaxy in the Swift/UVOT filters before detection of the X-ray transient.

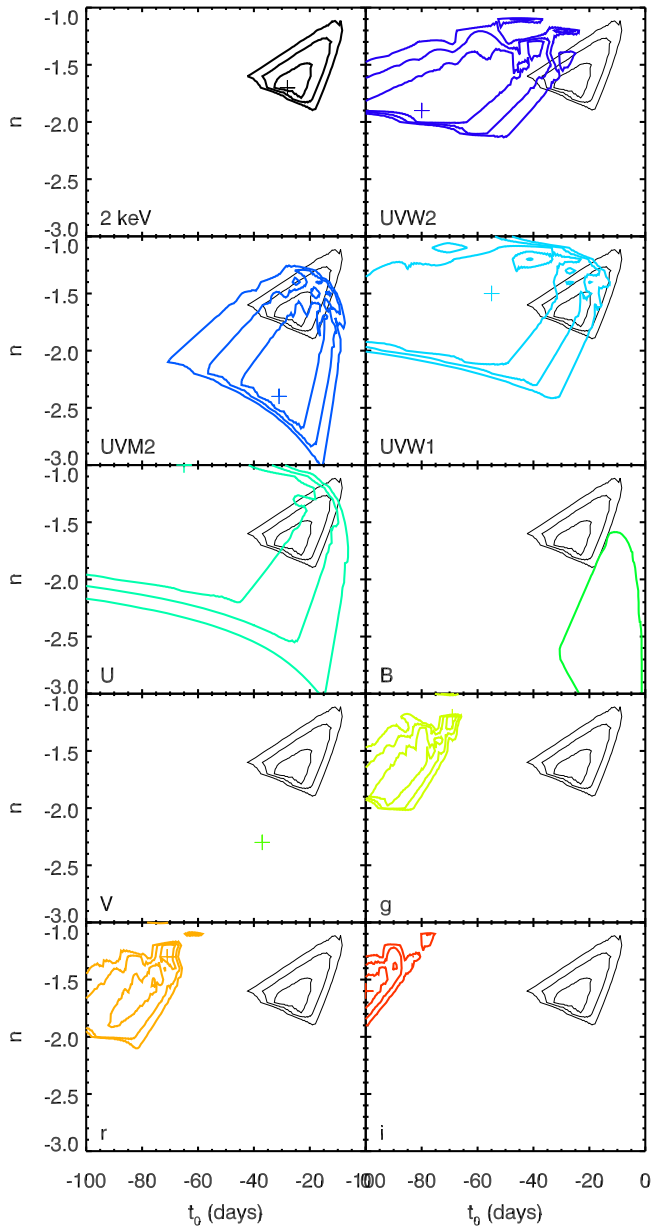


Figure 8. 1σ , 2σ , and 3σ χ^2 contours of the fits to the Swift/XRT, Swift/UVOT, and ZTF light curves. Plus signs mark the χ^2 minimum. The X-ray contours, plotted with black lines, are overplotted on the optical/UV ones for comparison.

Table 5
Light-curve Fitting Results

Band	n	t_0 (days)
X-ray (2 keV)	$-1.7^{+0.2}_{-0.1}$	-30^{+10}_{-5}
UV (UVW2)	$-1.9^{+0.5}_{-0.1}$	-80^{+40}_{-20}
Optical (i)	$-1.6^{+0.2}_{-0.1}$	<-90

Note. Results from the fit of a power-law decline model to the X-ray, UV, and optical light curves of the transient in SDSS J143359.16+400636.0.

of 456 Mpc, and is a factor of ~ 20 lower than the 0.5–15 keV luminosity measured at the same time (Section 2.2).

The $\Gamma = 1.0$ observed in the UVOT data is much flatter than the $\Gamma = 3.0$ observed in the X-ray band. For fitting the full SED, we use the χ^2 statistic and therefore grouped the X-ray

data with a minimum of 20 counts per bin. Furthermore, as with the X-ray-only data, we include a Galactic absorption component, fixed at $9.8 \times 10^{19} \text{ cm}^{-2}$ (HI4PI Collaboration et al. 2016), and an intrinsic absorption component, $z\text{tbabs}$, accounts for absorption at the redshift of the source and is left as a free parameter. The simplest model to fit the full SED is a broken power-law model where the break occurs at 1 keV, which yields a good fit where $\chi^2 = 114.62$ with 113 dof.

We then tried fitting a more physically motivated models, specifically a standard accretion disk model, `diskbb` in XSPEC (e.g., Mitsuda et al. 1984; Makishima et al. 1986). However, this model does not produce a good fit, where $\chi^2/\text{dof} = 2093.68/120$, fitting the ZTF and Swift/UVOT data well but severely underpredicting the X-ray data.

We then introduced a scattered power law in addition to the `diskbb` model, using the `simpl` model (Steiner et al. 2009). The `simpl` model is an empirical convolution model of Comptonization in which a fraction of the photons in an input seed spectrum, in this case the disk blackbody model, are upscattered into a power-law component. In XSPEC this is written as `simpl*diskbb`. This model accounts for the excess X-rays well, which significantly improves the model fit to $\chi^2/\text{dof} = 129.40/118$. The best-fit parameters of the disk model are an inner disk temperature of $T_{\text{in}} = 0.063^{+0.003}_{-0.007} \text{ keV}$ ($7.3^{+0.3}_{-0.8} \times 10^5 \text{ K}$) and a normalization of $N = 3.7^{+1.4}_{-1.0} \times 10^4$. The parameters of the scattered power law are $\Gamma = 3.2 \pm 0.1$ with a scattered fraction $f_{\text{scatt}} > 0.35$ (unconstrained at the upper end). The absorption intrinsic to the source is measured to be $N_{\text{H}} = (1.6 \pm 0.7) \times 10^{21} \text{ cm}^{-2}$. We summarize the SED fitting results in Table 6.

The normalization of the `diskbb` model described above is related to the apparent inner disk radius, where $N = (R_{\text{in}}/D_{10})^2 \cos \theta$. N is the normalization measured, D_{10} is the distance to the source in units of 10 kpc, and θ is the angle of the disk ($\theta = 0$ is face-on). Assuming a face-on disk and a distance of 456 Mpc to the source, the normalization of $3.7^{+1.4}_{-1.0} \times 10^4$ measured corresponds to an inner disk radius of $8.3 \times 10^9 \text{ km}$, or $3.8 \times 10^{10} \text{ km}$ for an edge-on disk ($\theta = 87^\circ$). The gravitational radius of a black hole with a mass of $\log(M_{\text{BH}}/M_{\odot}) = 7.41 \pm 0.41$ is $3.8 \times 10^{10} \text{ km}$. Therefore, the implied inner disk radius is consistent with the gravitational radius of the SMBH, given the uncertainty in the mass and the unknown disk inclination.

In addition to ruling out a relativistic jet from this source from the nondetection of radio emission, models of synchrotron emission, such as `srcut` and `sresc` in XSPEC, can reproduce the ZTF and Swift/UVOT data but have too much curvature in the X-ray band to fit the overall SED well. A bremsstrahlung model, such as `bremss`, also does not fit the spectrum well, being too steep for the ZTF and Swift/UVOT data and with too much curvature in the X-ray band. We therefore adopt the `simpl*diskbb` as our best-fit model.

In order to calculate the bolometric luminosity of the event, we integrated the flux of the unabsorbed/dereddened disk blackbody plus scattered power-law model over the 0.001–10 keV range. For the data taken at 8 days after the X-ray transient was detected by Swift described above, this yields $(2.3 \pm 0.3) \times 10^{-11} \text{ erg cm}^{-2} \text{ s}^{-1}$, which corresponds to a luminosity of $(5.7 \pm 0.1) \times 10^{44} \text{ erg s}^{-1}$ at a distance of 456 Mpc. Given the black hole mass of $\log(M_{\text{BH}}/M_{\odot}) = 7.41 \pm 0.41$ as measured from the stellar velocity dispersion, the Eddington luminosity of the SMBH is $3.1 \times 10^{45} \text{ erg s}^{-1}$;

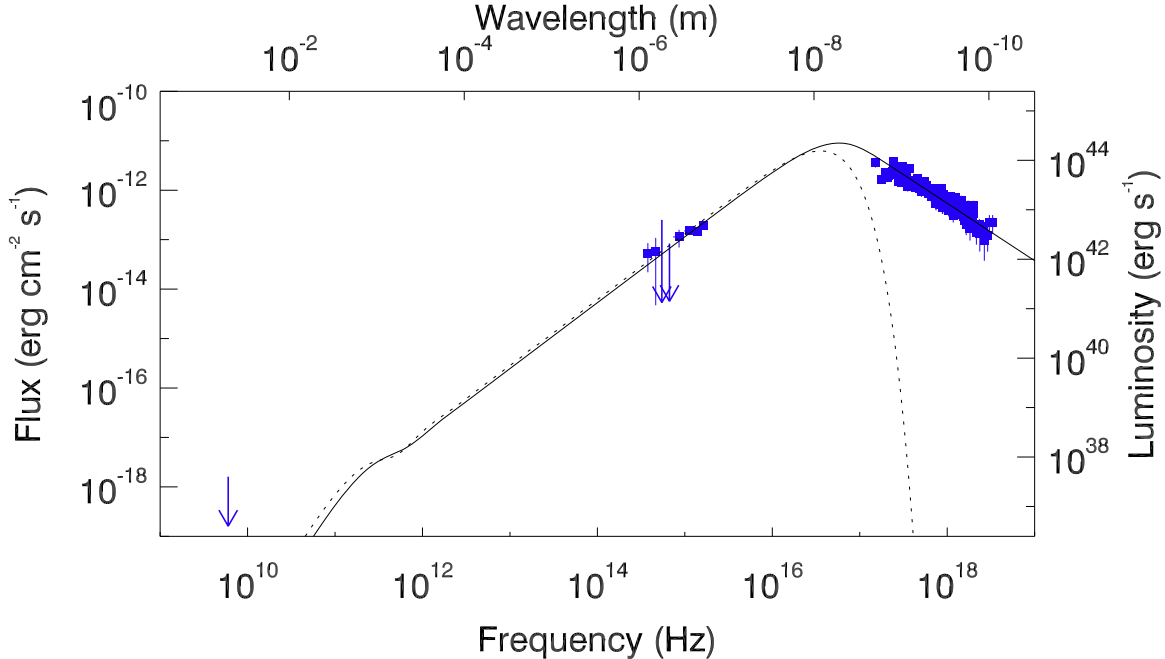


Figure 9. SED of the transient in SDSS J143359.16+400636.0 (blue data points), 8 days after it was detected by Swift, showing data from VLA, ZTF, Swift/UVOT, Chandra, and NuSTAR. The VLA data are from 172 days after the optical–X-ray data. Upper limits are shown with downward-pointing arrows. The best-fit dereddened and unabsorbed disk blackbody (`diskbb`; shown with a dashed line) plus power-law model is shown as a solid black line.

Table 6
SED Fitting Results

Parameter	Result
N_{H}	$(1.6 \pm 0.7) \times 10^{21} \mathrm{cm}^{-2}$
T_{in}	$0.063_{-0.007}^{+0.003} \mathrm{keV}$
Normalization	$3.7_{-1.0}^{+1.4} \times 10^4$
Γ	3.2 ± 0.1
f_{scatt}	>0.35
Flux (bolometric)	$(2.3 \pm 0.3) \times 10^{-11} \mathrm{erg cm}^{-2} \mathrm{s}^{-1}$
Luminosity (bolometric)	$(5.7 \pm 0.1) \times 10^{44} \mathrm{erg s}^{-1}$
χ^2	129.40
dof	118

Note. Results from the fit of a disk blackbody plus scattered power-law model to the ZTF, Swift/UVOT, NuSTAR, and Chandra data on the transient in SDSS J143359.16+400636.0 as measured on 2020 February 13, 8 days after the X-ray transient was first detected by Swift.

therefore, the Eddington fraction at this time was $\sim 10\%$. However, if we extrapolate the data back to when ZTF first detected the transient, when it was approximately five times more luminous in the optical bands, this implies that the Eddington fraction could have reached as high as 50%, if not greater.

8. The Host Galaxy SDSS J143359.16+400636.0

SDSS J143359.16+400636.0 is listed in SDSS with magnitudes $u = 20.76$, $g = 19.23$, $r = 18.56$, $i = 18.21$, and $z = 17.98$ (Alam et al. 2015) and in PanSTARRS with magnitudes $g = 18.72$, $r = 19.36$, $i = 18.97$, $z = 18.87$, and $y = 18.49$ (Chambers et al. 2016). In the infrared, Wide-field Infrared Survey Explorer (WISE) measured $W1 = 15.67$, $W2 = 15.43$, $W3 = 12.45$, and $W4 < 8.86$, and in the UV Galaxy Evolution Explorer measured $\mathrm{NUV} = 22.31$ (Bianchi et al. 2011).

As described in Section 5, neither the transient nor the galaxy was detected in the radio, with a 3σ upper limit of $28 \mu\mathrm{Jy}$ on the 6 GHz flux density. The VLA Faint Images of the Radio Sky at Twenty-cm (FIRST; Becker et al. 1995) survey, which covered the region with a sensitivity of 1 mJy at 1.4 GHz, also did not detect the galaxy.

No morphological type for the galaxy is reported in the literature; however, our Tractor fitting of the ZTF images finds that its brightness profile was better fit by a de Vaucouleurs profile than an exponential profile, implying that it is an elliptical galaxy.

The WISE colors of $W1 - W2 = 0.24$ are less than the $W1 - W2 \geq 0.8$ selection criterion of Stern et al. (2012) for AGNs, meaning that there was no evidence for the presence of a powerful AGN from the infrared in the galaxy prior to the X-ray transient. However, as described in Section 4, the optical line ratios revealed LINER activity in the nucleus.

SDSS J143359.16+400636.0 also has a companion galaxy, SDSS J143357.57+400647.3, which has an angular separation of $21''$ and a spectroscopic redshift of 0.0990 from SDSS. This angular distance corresponds to a projected separation of 38 kpc at this redshift, meaning that the two galaxies are likely interacting. The companion is brighter and visually larger on the sky, implying that it is the more massive of the two.

9. The Nature of the X-Ray Transient in SDSS J143359.16+400636.0

The X-ray transient in SDSS J143359.16+400636.0, with a peak luminosity of $\sim 10^{44} \mathrm{erg s}^{-1}$ and spatially coincident with the nucleus of the galaxy, is likely caused by an AGN flare or a TDE. Such events can be challenging to distinguish from each other (Auchettl et al. 2018). One specific example is IC 3599, which exhibited multiple X-ray flares that were interpreted both as AGN flares (Grupe et al. 2015) and as multiple tidal

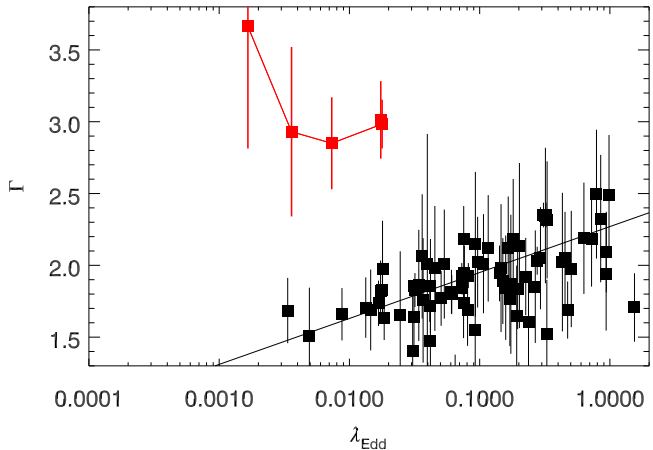


Figure 10. X-ray power-law index, Γ , of the X-ray transient in SDSS J143359.16+400636.0 plotted against its Eddington ratio, λ_{Edd} , and how it has varied over time (red data points). Data from a sample of AGNs presented in Brightman et al. (2013) are plotted for comparison (black data points), along with the statistically significant correlation found between these quantities (black line). This shows that Γ is not consistent with this property of AGNs, being too large for its λ_{Edd} .

disruption flares (Campana et al. 2015). We explore the likelihood of an AGN flare or a TDE in the following sections.

9.1. An AGN Flare in SDSS J143359.16+400636.0?

One of the distinguishing features of the X-ray transient in SDSS J143359.16+400636.0 is that the X-ray spectrum is soft, with $\Gamma \sim 3$, and the spectral shape does not appear to vary with time, even as the source luminosity dropped by an order of magnitude (Figure 2). These properties are in contrast to typical AGN properties, where the mean spectral index is $\Gamma = 1.8$ (e.g., Ricci et al. 2017), i.e., harder than observed for this transient. Furthermore, luminous AGNs usually show spectral evolution with a softer-when-brighter behavior (e.g., Sobolewska & Papadakis 2009; Auchettl et al. 2018), not seen for this source.

This softer-when-brighter behavior for AGNs also reveals itself in studies of the correlation between the X-ray power-law index, Γ , and the Eddington ratio, λ_{Edd} (e.g., Shemmer et al. 2006, 2008; Risaliti et al. 2009), but see Trakhtenbrot et al. (2017). For example, from a sample of 69 X-ray-bright sources in the Chandra Deep Field South and COSMOS surveys, Brightman et al. (2013) found that $\Gamma = (0.32 \pm 0.05) \log_{10} \lambda_{\text{Edd}} + (2.27 \pm 0.06)$. Given the observed peak Eddington ratio of 10% that we have calculated, Γ is expected to be ~ 1.8 , much lower than the value of 3 observed. We illustrate this in Figure 10, which shows the variation of Γ with λ_{Edd} for the X-ray transient in SDSS J143359.16+400636.0, along with the AGN data from Brightman et al. (2013). While narrow-line Seyfert 1 galaxies show steeper spectral slopes than other broad-lined AGNs (Brandt et al. 1997), similar to our source, they also show high Eddington ratios (e.g., Pounds et al. 1995), unlike our source.

Furthermore, for AGNs the bright quasar-like X-ray emission should be accompanied by bright UV emission, as predicted by the tight relationship between the X-ray and UV luminosities of quasars (e.g., Steffen et al. 2006; Lusso et al. 2010; Lusso & Risaliti 2016). Studies of this relationship usually parameterize these quantities by the monochromatic flux densities at 2 keV and 2500 Å. We use our fits to the light curve in Section 6 to calculate these quantities as a function of

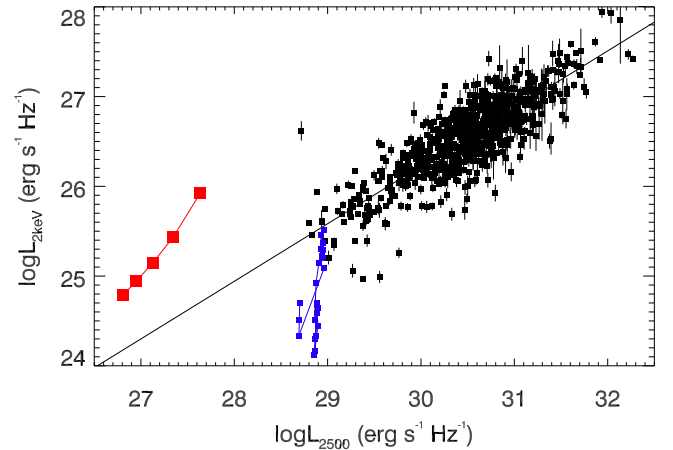


Figure 11. The 2 keV luminosity of the X-ray transient in SDSS J143359.16+400636.0, plotted against its luminosity at 2500 Å as a function of time (red data points representing data taken on 2020 February 5 and every 30 days after that). Data from 743 quasars selected from SDSS and 3XMM presented in Lusso & Risaliti (2016) are plotted for comparison (black data points), along with the statistically significant correlation they found between these quantities (black line). Also shown are data from a flare from the AGN Mrk 335 (blue points). These show that the X-ray luminosity of the transient is not consistent with the X-ray–UV properties of quasars, being too large for its UV luminosity.

time and plot them in Figure 11. Also plotted are data from 743 quasars selected from SDSS and 3XMM (Lusso & Risaliti 2016), along with the relation $\log L_2 \text{ keV} = 0.642 L_{2500} + 6.965$ derived from them.

At the observed peak of the transient, the rest-frame monochromatic flux at 2 keV was $3.4 \times 10^{-30} \text{ erg cm}^{-2} \text{ s}^{-1} \text{ Hz}^{-1}$, corresponding to a luminosity of $8.4 \times 10^{25} \text{ erg s}^{-1} \text{ Hz}^{-1}$ at $z = 0.099$, whereas the flux density at 2500 Å as determined from our SED fit is $1.7 \times 10^{-28} \text{ erg cm}^{-2} \text{ s}^{-1} \text{ Hz}^{-1}$, corresponding to a luminosity of $4.3 \times 10^{27} \text{ erg s}^{-1} \text{ Hz}^{-1}$ at this redshift. Given the relation $\log L_2 \text{ keV} = 0.642 L_{2500} + 6.965$ from 743 quasars selected from SDSS and 3XMM (Lusso & Risaliti 2016), the expected 2 keV luminosity of the X-ray transient in SDSS J143359.16+400636.0 given the measured 2500 Å one is $5.1 \times 10^{24} \text{ erg s}^{-1} \text{ Hz}^{-1}$, which is an order or magnitude less luminous than measured, indicating that the X-ray transient in SDSS J143359.16+400636.0 does not exhibit the UV–X-ray properties of AGNs.

However, the data from Lusso & Risaliti (2016) are from single-epoch observations of mostly steady-state AGNs that may not capture the properties of a flaring AGN that may be more appropriate. Auchettl et al. (2018) conducted a comparison between a sample of X-ray TDEs and a sample of flaring AGNs. The flaring AGN with most in common to SDSS J143359.16+400636.0 is Mrk 335, a narrow-line Seyfert galaxy at $z = 0.025$, whose flaring activity was revealed through long-term Swift observations (e.g., Gallo et al. 2018). In order to compare the X-ray to UV properties of the transient in SDSS J143359.16+400636.0 to an AGN flare, we take the Swift data presented in Gallo et al. (2018) and plot them in Figure 11. Here we have converted the XRT count rates to the 2 keV monochromatic flux density by assuming a power-law spectrum with $\Gamma = 2$, and we have used the UVW1 photometry to calculate the 2500 Å monochromatic fluxes. The range in X-ray luminosity of the flare from Mrk 335 is comparable to that observed from SDSS J143359.16+400636.0; however, the UV luminosity of the flare from Mrk 335 is ~ 2 orders of magnitude higher. This indicates that

the X-ray transient in SDSS J143359.16+400636.0 does not exhibit the UV–X-ray properties of this flaring AGN.

The presence of narrow emission lines in the optical spectrum with flux ratios common to LINER galaxies suggests that a low accretion rate AGN was present in this galaxy, at least 10^4 yr prior to the transient—this is how long it would have taken to illuminate the narrow-line region located on kiloparsec scales from the SMBH. The galaxy would also not be selected as an AGN with its WISE colors of $W1-W2 = 0.24$, which is less than the $W1-W2 \geq 0.8$ criterion of Assef et al. (2013). We also checked for historical AGN variability in the $W1$ and $W2$ bands by building a neoWISE (Mainzer et al. 2011) light curve between 2014 January 8 and 2019 June 18 and found no evidence of prior variability. Furthermore, the AGN luminosity inferred from the [O III] flux is lower than expected from the current X-ray luminosity. Therefore, while a low-luminosity AGN may have existed before the onset of this new activity, it is difficult to reconcile the X-ray and UV properties of this transient with the properties of the general AGN population, or indeed an AGN flare.

9.2. A TDE in SDSS J143359.16+400636.0?

The alternative solution is that this transient was a TDE. Auchettl et al. (2017) presented a comprehensive analysis of the X-ray emission from TDEs, and in Auchettl et al. (2018) they conducted a comparison between the X-ray properties of X-ray TDEs and flaring AGNs. Auchettl et al. (2017) stipulated several criteria for identifying an X-ray transient as a TDE. The ones that SDSS J143359.16+400636.0 satisfies are that the X-ray light curve has a well-defined shape and observable trend with several observations prior to the flare; the general shape of the X-ray light-curve decay is monotonically declining; the maximum luminosity detected from the event is at least two orders of magnitude larger than the X-ray upper limit immediately preceding the discovery of the flare; over the full time range of X-ray data available for the source of interest, the candidate TDE shows evidence of X-ray emission from only the flare, while no other recurrent X-ray activity is detected; and the X-ray flare is coincident with the nucleus of the host galaxy.

One further criterion states that the X-ray light curve shows a rapid increase in X-ray luminosity, which then declines on timescales of months to years. While the decline on timescales of months was observed, the rise of the X-ray transient in SDSS J143359.16+400636.0 was not. eROSITA detected the transient 40 days prior to Swift, but prior to that, the nearest X-ray observation to that was 4 yr earlier, also by Swift. The eROSITA measurement is also not consistent with the $t^{-5/3}$ as measured by Swift, but it is possible that this was part of the rise, and that the source peaked and declined before Swift detected it, or the light curve initially exhibited a plateau. This was seen in ASASSN-14li, where the X-ray light curve was constant for the first ~ 100 days, after which it followed the $t^{-5/3}$ decline (Holcinen et al. 2016; van Velzen et al. 2016; Brown et al. 2017).

Furthermore, Auchettl et al. (2017) stipulate that, based on its optical spectrum or other means, one finds no evidence of AGN activity arising from its host galaxy. We find LINER-like line ratios in the optical spectrum of SDSS J143359.16+400636.0, indicating low-level AGN activity prior to the event, so SDSS J143359.16+400636.0 does not strictly satisfy

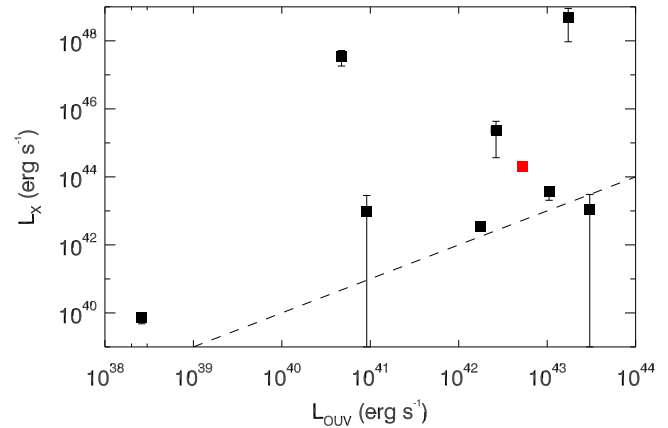


Figure 12. X-ray luminosity of the X-ray transient in SDSS J143359.16+400636.0, plotted against its optical/UV luminosity (red data point). Data from a sample of X-ray TDEs presented in Auchettl et al. (2017) are plotted for comparison (black data points). The dashed black line marks where the two quantities are equal. The X-ray luminosity with respect to the optical/UV luminosity for SDSS J143359.16+400636.0 is consistent with other X-ray TDEs.

this criterion. However, we note that several other TDEs have shown indications of prior AGN activity, including ASASSN-14li, as determined from a radio detection and a narrow [O III] line (van Velzen et al. 2016), and those shown in Figure 6.

Finally, we compare the optical/UV and X-ray luminosities of the X-ray transient in SDSS J143359.16+400636.0 to those presented for the X-ray TDEs in Auchettl et al. (2017) in Figure 12. This shows that the X-ray luminosity with respect to the optical/UV luminosity for SDSS J143359.16+400636.0 is consistent with other X-ray TDEs, albeit that these events present more diverse properties than AGNs.

In their comparison between the X-ray properties of X-ray TDEs and flaring AGNs, Auchettl et al. (2018) noted the lack of X-ray spectral evolution in TDEs, whereas AGNs often show significant spectral evolution, as we showed in the previous section. We therefore find that since the source satisfies most of the criteria for classifying X-ray TDEs set out by Auchettl et al. (2017), and that the X-ray and UV properties of the X-ray transient in SDSS J143359.16+400636.0 are more comparable to known TDEs than AGNs, we conclude that the transient likely is powered by a TDE.

10. The X-Ray Transient in SDSS J143359.16+400636.0 in the Context of TDEs

Of the 13 transients classified as X-ray TDEs or likely X-ray TDEs from the sample of Auchettl et al. (2017), most (10) were first detected in the X-ray band, either from XMM-Newton slews, serendipitously in Chandra or XMM-Newton pointed observations, or from hard X-ray monitors such as Swift/BAT. The other three were detected in optical surveys. Therefore, SDSS J143359.16+400636.0 adds to the number of TDEs first detected in the X-rays.

In comparison to these other TDEs, we find that SDSS J1201+30 is the event that shows most similarity to SDSS J143359.16+400636.0 in terms of its X-ray and optical/UV luminosities. It was also powered by a black hole of similar mass ($10^{7.2} M_\odot$; Wevers et al. 2019). SDSS J1201+30 was first detected by XMM-Newton during a slew with $L_X \sim 3 \times 10^{44} \text{ erg s}^{-1}$, which was 56 times brighter than a previous ROSAT upper limit and decayed with a $t^{-5/3}$ profile (Saxton

et al. 2012). A power-law fit to the X-ray spectrum of the source yielded $\Gamma = 3.38 \pm 0.04$. The optical/UV emission from this source was also weak, with 0.002–0.1 keV luminosity of $(2.64 \pm 0.31) \times 10^{42}$ erg s $^{-1}$ (Auchettl et al. 2017). The source also did not present broad or coronal optical lines. The X-ray spectrum could be reproduced with a bremsstrahlung or double-power-law model. These characteristics are similar to SDSS J143359.16+400636.0.

One property of SDSS J1201+30 that we do not see in SDSS J143359.16+400636.0 is variability on timescales of days in addition to the monotonic flux decline. SDSS J1201+30 became invisible to Swift between 27 and 48 days after discovery, which Saxton et al. (2012) suggested could be due to self-absorption by material driven from the system by radiation pressure during an early super-Eddington accretion phase. Alternatively, Liu et al. (2014) suggested that a supermassive black hole binary lies at the heart of SDSS J1201+30 and that the dips in the light curve were due to disruption of the accretion flow by the secondary SMBH. SDSS J143359.16+400636.0, however, does not show evidence for excess variability from the power-law decline.

In terms of how the X-ray light curve of SDSS J143359.16+400636.0 compares with the well-sampled X-ray light curves of other X-ray TDEs, SDSS J143359.16+400636.0 appears to have shown a plateau of emission before declining, similar to ASSASN-14li (van Velzen et al. 2016), while XMMSL1 J0740-85 declined monotonically without evidence for a plateau (Saxton et al. 2017).

Having compared the properties of the TDE in SDSS J143359.16+400636.0 to other X-ray TDEs, it is useful to compare the optical emission from the TDE in SDSS J143359.16+400636.0 to that of optically selected TDEs. For this we use the recent sample of 17 ZTF-discovered TDEs presented in van Velzen et al. (2021). Here the authors use a simple blackbody model to fit the optical/UV data of their sample. We proceed to fit the optical/UV data described in Section 7, finding that these can be described by a blackbody with $\log(T/K) = 4.3^{+0.2}_{-0.1}$, where the g -band luminosity is $\log(L_g/\text{erg s}^{-1}) = 41.0 \pm 0.1$ and the total blackbody luminosity is $\log(L_{\text{bb}}/\text{erg s}^{-1}) = 42.8 \pm 0.1$. While the temperature is comparable to the sample of van Velzen et al. (2021), which has the range $\log(T/K) = 4.1$ –4.6, the luminosities are much lower, where the ZTF TDEs have $\log(L_g/\text{erg s}^{-1}) = 42.8$ –43.6 and $\log(L_{\text{bb}}/\text{erg s}^{-1}) = 43.2$ –44.7.

The black hole mass inferred from the stellar velocity dispersion of SDSS J143359.16+400636.0 is $\sim 10^{7.4} M_{\odot}$, which is around the peak of the observed distribution of black hole masses of TDEs (Stone & Metzger 2016), although for optical events this was found to be lower, $\sim 10^6 M_{\odot}$ (Wevers et al. 2017). We calculated that the Eddington fraction of the event near peak was only $\sim 10\%$. This is naturally explained since the SMBH has a mass of $\sim 10^{7.4} M_{\odot}$, meaning that a very massive star would have been needed to reach Eddington luminosities. Strubbe & Quataert (2009) stated that TDEs can emit above the Eddington luminosity for a BH with $M_{\text{BH}} < 10^7 M_{\odot}$. Indeed, Stone & Metzger (2016) concluded that Eddington-limited emission channels of TDEs dominate the rates.

Finally, we noted that SDSS J143359.16+400636.0 has a companion galaxy, SDSS J143357.57+400647.3, which has a projected separation of 38 kpc. This may be important since a companion galaxy that may be undergoing an interaction

with the host could be relevant to the fueling of TDEs (French et al. 2020).

11. Implications and Conclusions

Only 13 transients were classified as X-ray TDEs or likely X-ray TDEs from the sample of Auchettl et al. (2017), so the number of known X-ray TDEs is still small. Therefore, finding more events of this nature is important for understanding this population, even just one event as we have reported here.

This TDE was one of a few identified where previous AGN activity in the galaxy was known, albeit at a low level. Other TDEs with known AGN activity prior to the flare include ASSASN-14li (van Velzen et al. 2016), where archival radio data and narrow [O III] emission showed that a low-luminosity AGN existed prior to the event. As can be seen in Figure 6, several other TDE hosts showed similar evidence for prior AGN activity from their narrow-line ratios, including CNSS J0019+00 (Sy2; Anderson et al. 2020). Furthermore, Ricci et al. (2020) postulated that a TDE caused the changing-look behavior of the AGN 1ES 1927+654, and Merloni et al. (2015) suggested that TDEs may be drivers of these changing-look events.

While we used ZTF data to determine the optical evolution of this TDE, this event was not identified as a TDE by wide-field optical surveys such as ZTF or ASAS-SN, possibly due to its low optical luminosity. We note, however, that ZTF was not observing the field of SDSS J143359.16+400636.0 when the optical luminosity was at its peak, which may be the reason it was missed. This TDE was also not classified as a TDE from its optical spectrum. Taken together, this suggests that many more events like it are being missed, and ultimately only wide-field UV or X-ray surveys will catch events like these. eROSITA is currently conducting an all-sky survey in the 0.2–10 keV band and will likely identify a large number of them (Merloni et al. 2012).

In conclusion, we have reported on an X-ray transient, observed to peak at a 0.3–10 keV luminosity of 10^{44} erg s $^{-1}$, originating in the nucleus of the galaxy SDSS J143359.16+400636.0 at $z = 0.099$. The X-ray transient was also accompanied by a less powerful optical/UV transient. A soft X-ray spectrum with $\Gamma = 3$ and the low UV/X-ray ratio disfavor an AGN flare scenario. The source was observed to decline monotonically in all bands, consistent with a $t^{-5/3}$ profile favoring a TDE scenario. Since this event was not identified as a TDE by wide-field optical surveys, or by optical spectroscopy, we are led to the conclusion that a significant fraction of X-ray TDEs may be going unnoticed.

The majority of this research and manuscript preparation took place during the COVID-19 global pandemic. The authors would like to thank all those who risked their lives as essential workers in order for us to safely continue our work from home.

We wish to thank the Swift PI, Brad Cenko, for approving the target of opportunity requests we made to observe SDSS J143359.16+400636.0, as well as the rest of the Swift team for carrying the observations out. We also acknowledge the use of public data from the Swift data archive.

We also wish to thank the NuSTAR PI, Fiona Harrison, for approving the DDT request we made to observe SDSS J143359.16+400636.0, as well as the NuSTAR SOC for carrying out the observation. This work was also supported under NASA contract No. NNG08FD60C. NuSTAR is a

project led by the California Institute of Technology, managed by the Jet Propulsion Laboratory, and funded by the National Aeronautics and Space Administration. This research has made use of the NuSTAR Data Analysis Software (NuSTARDAS) jointly developed by the ASI Science Data Center (ASDC, Italy) and the California Institute of Technology (USA).

ZTF is supported by the National Science Foundation under grant No. AST-1440341 and a collaboration including Caltech, IPAC, the Weizmann Institute for Science, the Oskar Klein Center at Stockholm University, the University of Maryland, the University of Washington, Deutsches Elektronen-Synchrotron and Humboldt University, Los Alamos National Laboratories, the TANGO Consortium of Taiwan, the University of Wisconsin at Milwaukee, and Lawrence Berkeley National Laboratories. Operations are conducted by COO, IPAC, and UW.

This paper is based on observations obtained with the Samuel Oschin Telescope 48-inch and the 60-inch Telescope at the Palomar Observatory as part of the Zwicky Transient Facility project. ZTF is supported by the National Science Foundation under grant No. AST-1440341 and a collaboration including Caltech, IPAC, the Weizmann Institute for Science, the Oskar Klein Center at Stockholm University, the University of Maryland, the University of Washington, Deutsches Elektronen-Synchrotron and Humboldt University, Los Alamos National Laboratories, the TANGO Consortium of Taiwan, the University of Wisconsin at Milwaukee, and Lawrence Berkeley National Laboratories. Operations are conducted by COO, IPAC, and UW. SED Machine is based on work supported by the National Science Foundation under grant No. 1106171.

The ZTF forced-photometry service was funded under the Heising-Simons Foundation grant No. 12540303 (PI: Graham).

Facilities: Swift (XRT, UVOT), NuSTAR, CXO, Keck:I (LRIS), PO:1.2 m PO:1.5 m, VLA.

Software: CASA (McMullin et al. 2007), CIAO (Fruscione et al. 2006), 1pipe (Perley 2019), The Tractor (Lang et al. 2016), XSPEC (Arnaud 1996).

ORCID iDs

Murray Brightman  <https://orcid.org/0000-0002-8147-2602>
 Daniel Stern  <https://orcid.org/0000-0003-2686-9241>
 Kunal Mooley  <https://orcid.org/0000-0002-2557-5180>
 Suvi Gezari  <https://orcid.org/0000-0003-3703-5154>
 Sjoert Van Velzen  <https://orcid.org/0000-0002-3859-8074>
 Matthew Graham  <https://orcid.org/0000-0002-3168-0139>
 Frank J. Masci  <https://orcid.org/0000-0002-8532-9395>
 Reed Riddle  <https://orcid.org/0000-0002-0387-370X>

References

Alam, S., Albareti, F. D., Allende Prieto, C., et al. 2015, *ApJS*, 219, 12
 Alexander, K. D., van Velzen, S., Horesh, A., & Zauderer, B. A. 2020, *SSRv*, 216, 81
 Anderson, M. M., Mooley, K. P., Hallinan, G., et al. 2020, *ApJ*, 903, 116
 Arnaud, K. A. 1996, in *ASP Conf. Ser.* 101, *Astronomical Data Analysis Software and Systems V*, ed. G. H. Jacoby (San Francisco, CA: ASP), 17
 Assef, R. J., Stern, D., Kochanek, C. S., et al. 2013, *ApJ*, 772, 26
 Auchettl, K., Guillochon, J., & Ramirez-Ruiz, E. 2017, *ApJ*, 838, 149
 Auchettl, K., Ramirez-Ruiz, E., & Guillochon, J. 2018, *ApJ*, 852, 37
 Becker, R. H., White, R. L., & Helfand, D. J. 1995, *ApJ*, 450, 559
 Bellm, E. C., Kulkarni, S. R., Graham, M. J., et al. 2019, *PASP*, 131, 018002
 Berney, S., Koss, M., Trakhtenbrot, B., et al. 2015, *MNRAS*, 454, 3622
 Bianchi, L., Herald, J., Efremova, B., et al. 2011, *Ap&SS*, 335, 161
 Boller, T., Freyberg, M. J., Trümper, J., et al. 2016, *A&A*, 588, A103
 Brandt, W. N., Mathur, S., & Elvis, M. 1997, *MNRAS*, 285, L25
 Brightman, M., Silverman, J. D., Mainieri, V., et al. 2013, *MNRAS*, 433, 2485
 Brown, J. S., Holoien, T. W. S., Auchettl, K., et al. 2017, *MNRAS*, 466, 4904
 Burrows, D. N., Hill, J. E., Nousek, J. A., et al. 2005, *SSRv*, 120, 165
 Campana, S., Mainetti, D., Colpi, M., et al. 2015, *A&A*, 581, A17
 Cappellari, M. 2017, *MNRAS*, 466, 798
 Cappellari, M., & Emsellem, E. 2004, *PASP*, 116, 138
 Chambers, K. C., Magnier, E. A., Metcalfe, N., et al. 2016, arXiv:1612.05560
 Chen, J., Shi, Y., Dempsey, R., et al. 2019, *MNRAS*, 489, 855
 Evans, C. R., & Kochanek, C. S. 1989, *ApJL*, 346, L13
 Evans, P. A., Beardmore, A. P., Page, K. L., et al. 2007, *A&A*, 469, 379
 Evans, P. A., Beardmore, A. P., Page, K. L., et al. 2009, *MNRAS*, 397, 1177
 French, K. D., Arcavi, I., & Zabludoff, A. 2016, *ApJL*, 818, L21
 French, K. D., Arcavi, I., & Zabludoff, A. 2017, *ApJ*, 835, 176
 French, K. D., Wevers, T., Law-Smith, J., Graur, O., & Zabludoff, A. I. 2020, *SSRv*, 216, 32
 Fruscione, A., McDowell, J. C., Allen, G. E., et al. 2006, *Proc. SPIE*, 6270, 62701V
 Gaia Collaboration, Brown, A. G. A., Vallenari, A., et al. 2018, *A&A*, 616, A1
 Gallo, L. C., Blue, D. M., Grupe, D., Komossa, S., & Wilkins, D. R. 2018, *MNRAS*, 478, 2557
 Graham, M. J., Kulkarni, S. R., Bellm, E. C., et al. 2019, *PASP*, 131, 078001
 Grupe, D., Komossa, S., & Saxton, R. 2015, *ApJL*, 803, L28
 Harrison, F. A., Craig, W. W., Christensen, F. E., Hailey, C. J., & Zhang, W. W. 2013, *ApJ*, 770, 103
 HI4PI Collaboration, Ben Bekhti, N., Flöer, L., et al. 2016, *A&A*, 594, A116
 Ho, A. Y. Q., Kulkarni, S. R., Perley, D. A., et al. 2020, *ApJ*, 902, 86
 Holoien, T. W. S., Kochanek, C. S., Prieto, J. L., et al. 2016, *MNRAS*, 455, 2918
 Holoien, T. W. S., Valley, P. J., Auchettl, K., et al. 2019, *ApJ*, 883, 111
 Kauffmann, G., Heckman, T. M., Tremonti, C., et al. 2003, *MNRAS*, 346, 1055
 Kewley, L. J., Heisler, C. A., Dopita, M. A., & Lumsden, S. 2001, *ApJS*, 132, 37
 Khabibullin, I., Sunyaev, R., Churazov, E., et al. 2020, *ATel*, 13494, 1
 Komossa, S. 2015, *JHEAp*, 7, 148
 Lang, D., Hogg, D. W., & Myktyn, D. 2016, *The Tractor: Probabilistic Astronomical Source Detection and Measurement DR9.4*, *Astrophysics Source Code Library*, ascl:1604.008
 Law-Smith, J., Ramirez-Ruiz, E., Ellison, S. L., & Foley, R. J. 2017, *ApJ*, 850, 22
 Liu, F. K., Li, S., & Komossa, S. 2014, *ApJ*, 786, 103
 Lusso, E., Comastri, A., Vignali, C., et al. 2010, *A&A*, 512, A34
 Lusso, E., & Risaliti, G. 2016, *ApJ*, 819, 154
 Madsen, K. K., Harrison, F. A., Markwardt, C. B., et al. 2015, *ApJS*, 220, 8
 Mainzer, A., Bauer, J., Grav, T., et al. 2011, *ApJ*, 731, 53
 Makishima, K., Maejima, Y., Mitsuda, K., et al. 1986, *ApJ*, 308, 635
 Masci, F. J., Laher, R. R., Rusholme, B., et al. 2019, *PASP*, 131, 018003
 Mattila, S., Pérez-Torres, M., Efstathiou, A., et al. 2018, *Sci*, 361, 482
 McMullin, J. P., Waters, B., Schiebel, D., Young, W., & Golap, K. 2007, in *ASP Conf. Ser.* 376, *Astronomical Data Analysis Software and Systems XVI*, ed. R. A. Shaw (San Francisco, CA: ASP), 127
 Merloni, A., Dwelly, T., Salvato, M., et al. 2015, *MNRAS*, 452, 69
 Merloni, A., Predehl, P., Becker, W., et al. 2012, arXiv:1209.3114
 Mitsuda, K., Inoue, H., Koyama, K., et al. 1984, *PASJ*, 36, 741
 Oke, J. B., Cohen, J. G., Carr, M., et al. 1995, *PASP*, 107, 375
 Perley, D. A. 2019, *PASP*, 131, 084503
 Pounds, K. A., Done, C., & Osborne, J. P. 1995, *MNRAS*, 277, L5
 Rees, M. J. 1988, *Natur*, 333, 523
 Ricci, C., Kara, E., Loewenstein, M., et al. 2020, *ApJL*, 898, L1
 Ricci, C., Trakhtenbrot, B., Koss, M. J., et al. 2017, *ApJS*, 233, 17
 Risaliti, G., Salvati, M., Elvis, M., et al. 2009, *MNRAS*, 393, L1
 Saxton, R. D., Read, A. M., Esquej, P., et al. 2008, *A&A*, 480, 611
 Saxton, R. D., Read, A. M., Esquej, P., et al. 2012, *A&A*, 541, A106
 Saxton, R. D., Read, A. M., Komossa, S., et al. 2017, *A&A*, 598, A29
 Shemmer, O., Brandt, W. N., Netzer, H., Maiolino, R., & Kaspi, S. 2006, *ApJL*, 646, L29
 Shemmer, O., Brandt, W. N., Netzer, H., Maiolino, R., & Kaspi, S. 2008, *ApJ*, 682, 81
 Sobolewska, M. A., & Papadakis, I. E. 2009, *MNRAS*, 399, 1597
 Soderberg, A., Grindlay, J. E., Bloom, J. S., et al. 2009, *Astro2010: The Astronomy and Astrophysics Decadal Survey*, Vol. 2010 (Washington, DC: The National Academies of Sciences, Engineering, and Medicine), 278
 Steffen, A. T., Strateva, I., Brandt, W. N., et al. 2006, *AJ*, 131, 2826

Steiner, J. F., Narayan, R., McClintock, J. E., & Ebisawa, K. 2009, *PASP*, **121**, 1279

Stern, D., Assef, R. J., Benford, D. J., et al. 2012, *ApJ*, **753**, 30

Stone, N. C., & Metzger, B. D. 2016, *MNRAS*, **455**, 859

Strubbe, L. E., & Quataert, E. 2009, *MNRAS*, **400**, 2070

Trakhtenbrot, B., Ricci, C., Koss, M. J., et al. 2017, *MNRAS*, **470**, 800

Tremonti, C. A., Heckman, T. M., Kauffmann, G., et al. 2004, *ApJ*, **613**, 898

van Velzen, S., Anderson, G. E., Stone, N. C., et al. 2016, *Sci*, **351**, 62

van Velzen, S., Gezari, S., Cenko, S. B., et al. 2019, *ApJ*, **872**, 198

van Velzen, S., Gezari, S., Hammerstein, E., et al. 2021, *ApJ*, **908**, 4

Voges, W., Aschenbach, B., Boller, T., et al. 1999, *A&A*, **349**, 389

Weisskopf, M. C. 1999, arXiv:[astro-ph/9912097](https://arxiv.org/abs/astro-ph/9912097)

Wevers, T., Stone, N. C., van Velzen, S., et al. 2019, *MNRAS*, **487**, 4136

Wevers, T., van Velzen, S., Jonker, P. G., et al. 2017, *MNRAS*, **471**, 1694

Woo, J.-H., Schulze, A., Park, D., et al. 2013, *ApJ*, **772**, 49